修士学位論文

Development of Low Noise Electronics for the Measurement of the Magnetic Moment of the Antiproton

（反陽子磁気モーメント測定のための低ノイズエレクトロニクスの開発）

広域科学専攻　相関基礎科学系
学籍番号： 31-126930
長濱　弘季

Abstract

The Baryon Antibaryon Symmetry Experiment (BASE) aims for a high-precision measurement of the magnetic moment (g-factor) of the antiproton at CERN, Geneva, Switzerland. To this end, we prepare a single particle in a cryogenic Penning trap. All information about a particle stored in such a trap is obtained by detecting image currents, which are induced by the interaction between the particle and the trap electrodes. In principle, the magnetic moment of the antiproton is determined by measuring the image currents using highly sensitive superconducting resonant detectors. The precision which can be achieved in the measurement depends mostly on the quality of those detectors.

During my master thesis studies, I developed such detection systems at frequencies between 600 kHz and 800 kHz for the measurement of the axial oscillation frequency of a single trapped antiproton. The detectors are based on superconducting resonators and ultra-low noise amplifiers. In addition, I developed low noise electronics, such as filter-boards to clean spurious RF noise from the highly stable DC voltage supply, which is used to bias the trap electrodes, as well as a temperature stabilization loop for the voltage source.

In this thesis, the principle of the experiment and my contributions to successful operation are described.

Contents

List of Figures

List of Tables

Chapter 1

Introduction

The motivation of the BASE experiment is to measure the antiproton g-factor with high precision to perform a stringent test of the CPT symmetry; the most fundamental symmetry in the Standard Model of particle physics. The CPT operation is the simultaneous transformation of charge, parity, and time. As a consequence, the CPT symmetry states that the fundamental properties of matter and antimatter must be identical. One example is that antiproton and proton magnetic moments have opposite signs but exactly the same value. Therefore, high-precision comparison of the magnetic moments of the proton and the antiproton provides a stringent test of CPT symmetry.

Many experiments to improve the precision of the proton magnetic moment were carried out. The first measurement was performed by Stern in the early 1930's, using the molecular beam techniques [1][2]. Further developments with molecular beams by Rabi improved the precision [3]. In the following decade, Purcell and Bloch developed nuclear magnetic resonance [4][5], which led to a further improvement. Afterwards, further progress was made by Ramsey and Kleppner, determined from hyperfine spectroscopy of atomic hydrogen [6][7]. In 1972, Kleppner improved the hydrogen maser technique and obtained 10 ppb precision, which is to date the most precise measurement of the proton magnetic moment [8][9]. However, exciting progress towards a direct measurements of the proton magnetic moment was achieved. The BASE companion experiment at the University of Mainz demonstrated very recently the application of the double Penning trap technique, which is a major step towards a high precision measurement of the proton magnetic moment at the ppb level.

Compared to the proton, there were only a few attempts to measure the antiproton magnetic moment. The measurement of the antiproton magnetic moment was carried out in 1988 and 2009 by using super-hyperfine spectroscopy of antiprotonic helium atoms (3000 ppm) [10][11]. Recently, the new best value was determined by a group of Harvard university in 2013 by using the first single-antiproton measurement with a cryogenic Penning trap (4.4 ppm) [12]. However, it is known the magnetic moments can be determined in Penning traps with much higher precision [13][14].

The BASE collaboration at CERN also aims for a high-precision measurement by utilizing Penning trap systems. Advantages and features of Penning trap sytems are as following: First, a single particle can be stored for arbitrarily long time. Second, the motional energy of a stored particle can be cooled down below 100 μeV and can be constrained to a tiny volume of $<$100 μm^3. Therefore, corrections due to the particle-particle interaction, thermal line-broadening, and interactions with the apparatus are negligible. In addition, aiming for a boost of precision, the so-called double Penning trap scheme, developed at the University of Mainz [15] will be applied. Moreover, to extract the magnetic moment with high precision, it requires low noise detection systems with ultra-high sensitivity. The detectors are based on superconducting resonators and ultra-low noise amplifiers. For my master studies, I mainly contributed to the development of such detection systems. Eventually, it is expected to provide an unprecedented precision of the antiproton magnetic moment, at the level of 1 ppb or better.

In chapter 2, theoretical aspects of the antiproton g-factor measurement are presented. In chapter 3, our experimental apparatus is described. In chapter 4, principles of detection systems are discussed, and its characterization is presented in chapter 5. In chapter 6, the characterization of the ultra-high precision voltage source for biasing the trap electrodes is described.

Chapter 2

Measurement of the antiproton g-factor

Aiming for measuring the antiproton g-factor with ultra-high precision, the BASE collaboration uses cryogenic Penning traps. The key for such an experiment is to confine a particle with extremely long observation time. Penning traps satisfy this requirement, and it is considered as the most stabilized tool for confining a single charged particle. The famous electron g-factor measurement is the most precise measurement using single trapped particles up to now [13]. In the first part of this chapter, the behavior of a single particle stored in a Penning trap is presented. Afterwards, the double trap method will be described.

§ 2.1 Particle motion in a Penning trap

In a magnetic field B, a particle of mass m and charge q is constrained to a circular orbit. This is the so-called "free-cyclotron motion". Choosing the z axis to be parallel or antiparallel to $\boldsymbol{B}$, the cyclotron orbit is a rotation obeying the right-hand rule. Its frequency is given by:

$$\omega_c = \frac{|q\boldsymbol{B}|}{m}. \tag{2.1}$$

The cyclotron motion is a radial motion, thus it is bound radially but not axially. In a Penning trap, an electrostatic quadrupole potential is superimposed to confine a particle also in the axial direction. The electric and magnetic field configuration of a Penning trap is shown in Fig. 2.1.

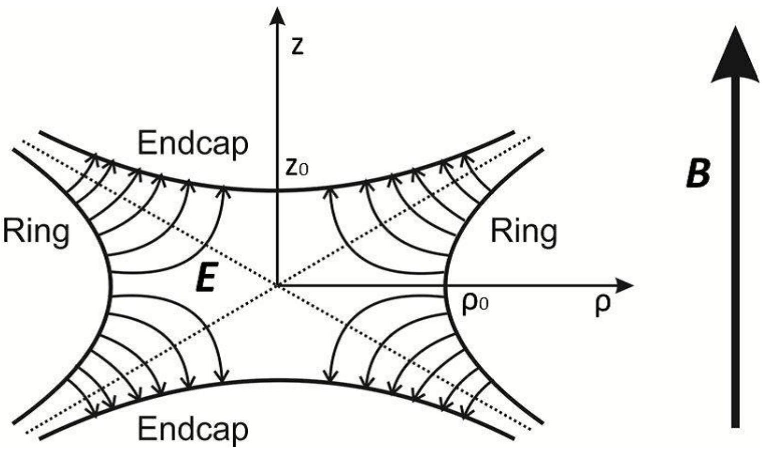

Fig. 2.1: Electric/magnetic field configuration of a Penning trap. The magnetic field confines a particle only in a radial direction. Together with the electrostatic quadrupole potential, it makes possible to confine a particle also in the axial direction. In total, three electrodes are required to generate the quadrupole potential. Two end cap electrodes on the top and the bottom, and one ring electrode in the center.

As shown in Fig. 2.1, three electrodes are required to generate the quadrupole potential: two endcap electrodes with one ring electrode in the center. The two endcap electrodes and the ring electrode are expressed as the hyperbola of revolution.

$$z^2 = z_0^2 + \rho^2/2 \tag{2.2}$$

$$z^2 = \frac{1}{2}(\rho^2 - \rho_0^2) \tag{2.3}$$

The electrostatic force given by a quadrupole potential can be written as:

$$V = V_0 C_2 (z^2 - \frac{\rho^2}{2}), \tag{2.4}$$

where V_0 is the potential difference between the endcap and the ring electrodes, and $\sqrt{C_2}$ a specific coefficient characterizing the typical geometrical length scale of the trap. An example of a three dimension plot of equation (2.4) is shown in Fig. 2.2.

This provides stable storage of a charged particle with a harmonic oscillation frequency of:

$$\omega_z = \sqrt{\frac{2qC_2V_0}{m}}. \tag{2.5}$$

Solving the full equation of motion of a particle in such a field configuration leads to a modification of the free cyclotron motion [16]. This is caused by the radial field compo-

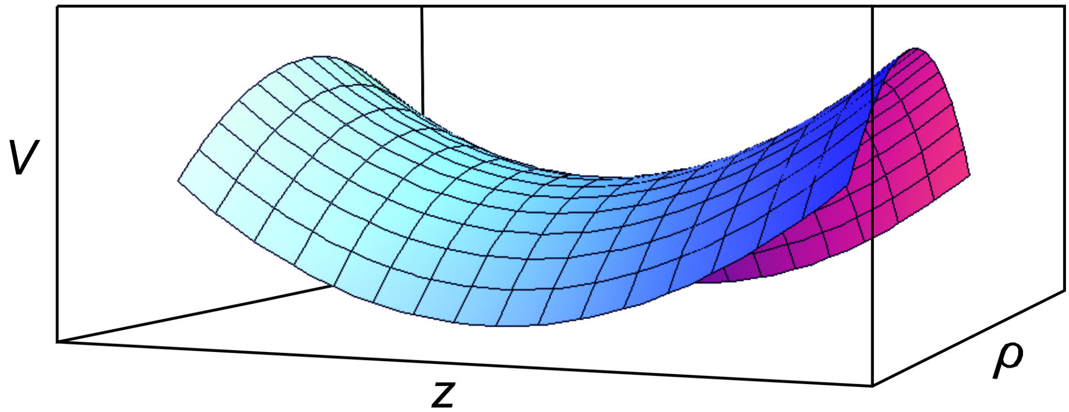

Fig. 2.2: Example of the electrostatic quadrupole potential. It can be verified that there is a harmonic potential in the axial direction (z axis). This allows to confine a particle in the axial direction, however, as it is obvious from this figure, confining in the radial direction (ρ direction) is impossible. By superimposing a homogeneous magnetic field (parallel or antiparallel to the z axis), it also confines in the radial direction.

nent of the electrostatic quadrupolar potential. The resulting eigen-frequency ω_+ of this modified cyclotron motion is

$$\omega_+ = \frac{1}{2}(\omega_c + \sqrt{\omega_c^2 - 2\omega_z^2}). \tag{2.6}$$

In addition, the so-called "magnetron motion" occurs, which is the second radial eigen-motion caused by a $\boldsymbol{E} \times \boldsymbol{B}$ drift. The magnetron frequency ω_- is

$$\omega_- = \frac{1}{2}(\omega_c - \sqrt{\omega_c^2 - 2\omega_z^2}) \approx \frac{V_0 C_2}{B}. \tag{2.7}$$

To first order, ω_- is independent on the properties of the trapped particle. It only depends on the electromagnetic fields. For $\omega_0^2 > 2\omega_z^2$, the Penning trap provides stable trapping conditions. Typical precision Penning traps are operated with parameters:

$$\omega_+ \gg \omega_z \gg \omega_-. \tag{2.8}$$

Some useful relations between the eigen-frequencies are

$$\omega_- = \frac{\omega_z^2}{2\omega_+} \tag{2.9}$$

$$\omega_c = \omega_+ + \omega_- \tag{2.10}$$

$$\omega_c^2 = \omega_+^2 + \omega_-^2 + \omega_z^2. \tag{2.11}$$

Equation (2.9) and (2.10) only hold for ideal Penning traps, whereas equation (2.11) is also valid in presence of specific trap errors [17]. Specifically this so-called invariance theorem makes Penning traps to strong tools in high-precision investigations of single particle properties.

Experimentally, the Penning trap is a stack of gold-plated copper electrodes mounted in the field of a superconducting magnet. The electrodes are electrically separated with insulating sapphire rings.

§ 2.2 The g-factor measurement

The g-factor is a dimensionless quantity which relates the spin $\vec{S}$ of a particle to its magnetic moment

$$\vec{\mu_s} = g\frac{q}{2m}\vec{S}, \tag{2.12}$$

where q is the charge, and m the mass of a particle, respectively. The spin energy of a particle E_s in the presence of a magnetic field $\vec{B_z}$ is

$$E_s = -\vec{\mu_s} \cdot \vec{B_z}. \tag{2.13}$$

Inserting equation (2.12) into equation (2.13) and using the spin eigen-values $\langle s_z \rangle = \pm\hbar/2$, the following equations are obtained:

$$E_s = \pm g\frac{q}{2m}\frac{\hbar}{2}B_z \tag{2.14}$$

$$\Delta E_s = g\frac{q\hbar}{2m}B_z, \tag{2.15}$$

where ΔE_s is the energy difference between the two spin states. It corresponds to the energy of the spin precession in the magnetic field. This is called the Larmor precession with its frequency:

$$\omega_L = g\frac{q}{2m}B_z. \tag{2.16}$$

Together with equation (2.1), the g-factor can be expressed as the ratio of the Larmor frequency ω_L and the free cyclotron frequency ω_c:

$$\omega_L = g \cdot \frac{\omega_c}{2} \iff g = 2\frac{\omega_L}{\omega_c}. \tag{2.17}$$

By measuring the three eigen-motions of the antiproton in a Penning trap and applying the invariance theorem (equation (2.11)), the free cyclotron motion ω_c is obtained. On the other hand, the Larmor frequency ω_L is determined by applying the continuous Stern-Gerlach effect, which is discussed in the following subsection.

§ 2.3 Determination of the Larmor frequency using the continuous Stern-Gerlach effect

The Larmor frequency ω_L can be measured by using the continuous Stern-Gerlach effect [18]. This elegant priniciple allows the non-destructive detection of the spin eigenstate. By superimposing a magnetic bottle B_2 to the Penning trap, the magnetic field can be expressed as:

$$B_z = B_0 + B_2 \left(z^2 - \frac{\rho^2}{2} \right). \tag{2.18}$$

By inserting this equation into equation (2.13), it can be verified that the magnetic bottle adds a spin dependent quadratic axial potential. Therefore, the magnetic moment of the antiproton will be coupled to its axial oscillation frequency. This allows the determination of the spin state by measuring the axial frequency. As illustrated in Fig. 2.3, this frequency becomes a function of the spin eigen-state of the antiproton. In the "spin-down" state the axial frequency of the trapped antiproton is lower than in the "spin-up" state. This is the main feature of the continuous Stern-Gerlach effect.

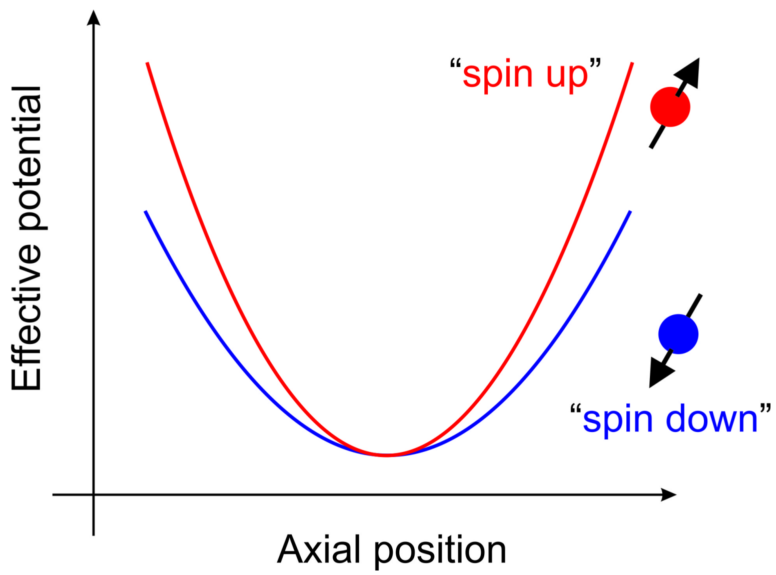

Fig. 2.3: Illustration of the continuous Stern-Gerlach effect for a single antiproton. In the presence of a magnetic field inhomogeneity $B_z = B_0 + B_2 z^2$, the axial frequency becomes a function of the spin eigen-state.

The axial frequency is measured and subsequently a spin flip transition is driven by the Rabi resonance principle [19]. Afterwards, the axial frequency is measured again. When the spin flip occurred, the axial frequency immediately changes by $\pm\Delta\nu_z$.

$$\pm\Delta\nu_z = \pm\frac{1}{2\pi^2}\frac{\mu_p B_2}{m\nu_z} \tag{2.19}$$

Repeating this sequence several times for different spin flip drive frequencies, the spin flip probability as a function of the drive frequency will be obtained. The Larmor frequency ω_L will be extracted from the peak of the resulting resonance curve.

This scheme was introduced by Dehmelt and Eckstrom [18], and has been used for measuring particles with magnetic moment at the level of the Bohr magneton. We will apply this technique to measure the antiproton magnetic moment [20]. However, the application of this principle to hadrons is an extremely challenging task.

For the (anti)proton, μ_p/m is more than one million times smaller compared to the electron (positron). This is the major difficulty of the experiment. The only solution for this is to superimpose a very strong magnetic bottle so as to increase $\Delta\nu_z$ as much as possible. To this end, we superimpose to our trap a magnetic bottle of B_2=300000 T/m^2, which leads to an antiproton spin flip shifts the axial frequency by 190 mHz out of 700 kHz.

§ 2.4 Double Penning trap technique

In the magnetic bottle, the Larmor frequency ω_L depend on the motional amplitudes:

$$\omega_L = \frac{gq}{2m}\left(B_0 + B_2\left(z_2 - \frac{\rho^2}{2}\right)\right), \tag{2.20}$$

which leads the g-factor resonance broaden. To overcome this problem, the spin state analysis and the free cyclotron frequency ω_c/Larmor frequency ω_L measurements are separated. In the so-called Analysis Trap (AT), the magnetic bottle is superimposed and the spin eigen-state is determined by the Stern-Gerlach effect as described in the previous subsection. The so-called Precision Trap (PT) has a high homogeneous magnetic field and the frequency measurement is affected by the magnetic bottle since it is spatially separated from the AT. The cyclotron frequency ω_c will be determined in the PT. In Fig. 2.4, it shows a procedure of the double Penning trap technique.

First, the spin flip drive is irradiated and the axial frequency is measured at the AT. From this procedure, the spin eigen-state of a particle will be determined. Subsequently, the antiproton will be transported to the PT and the axial frequency is measured again. Then, ω_c measurement is carried out and the spin flip drive at ν_{rf} is irradiated simultaneously. After transported back to the AT, the axial frequency is measured and subsequently a spin flip drive is irradiated. Thereby, the spin eigen-state is determined again. From this method, it is possible to conclude whether the spin has flipped by the RF drive ν at the PT or not. This sequence is repeated over several hundred times and a resonance curve of the spin-flip probability as a function of the drive frequency nu_{rf} is obtained. This scheme prevents the limitation of the experimental precision and it significantly reduces the line width of the g-factor resonance. This technique was applied successfully in g-factor measurements of the electron bound to highly charged ions, where experimental precisions at the sub-ppb level were achieved [14][21][22].

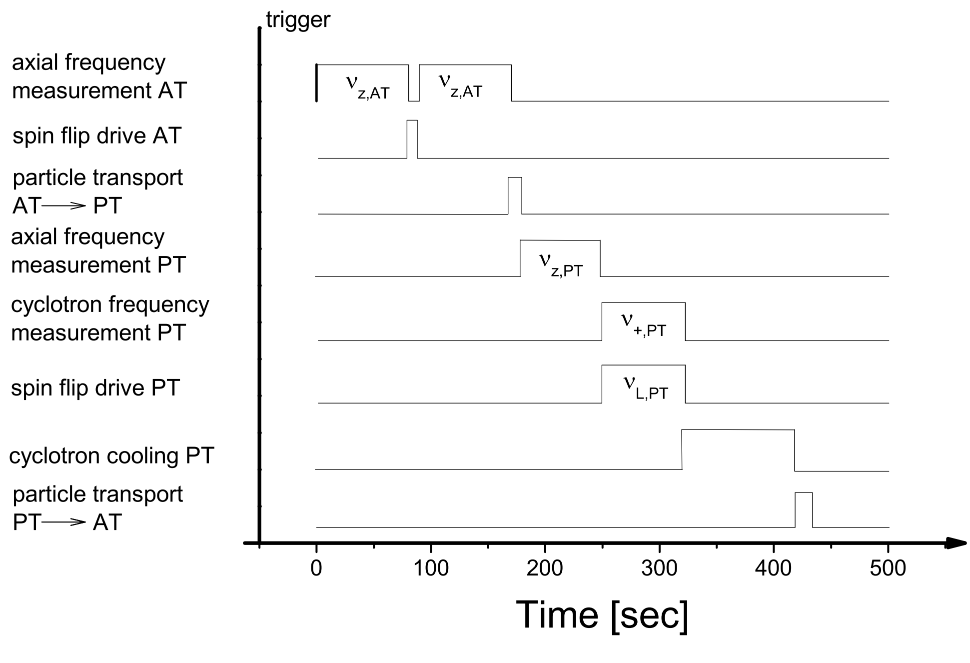

Fig. 2.4: Temporal sequence of the double Penning trap technique.

Chapter 3

Experimental setup

§ 3.1 Overview

The experimental apparatus consists of a superconducting magnet with a horizontal cylindrical bore as shown in Fig. 3.1. The Penning trap stack will be located in the homogeneous region of the magnetic field of the magnet, and is housed in a small indium sealed cryogenic cylindrical vacuum chamber. At the upstream side this cryogenic inner vacuum chamber is hermetically sealed with a degrader foil [23]. Background pressures on the order of 10^{-17} mbar can be achieved in this system [23], which ensures long storage times of the antiprotons. Moreover, the cryogenic conditions have the big advantage that active electronics noise are reduced. The cryogenic temperatures are provided by two cryostats mounted at the upstream and the downstream side of the magnet. The upstream side of the apparatus will be connected to the antiproton beamline, whereas the downstream side provides the interface to the room temperature electronics including voltage sources, RF amplifiers and down-converters. Eventually, the whole apparatus will be housed in a temperature stabilized Faraday cage.

Fig. 3.2 shows a cross section of the apparatus. Both cryostats contain two 35 liter tanks, one for liquid nitrogen and the other one for liquid helium. A 77 K thermal shield will be connected to the liquid nitrogen reservoir. The shield will be fixed to the 300 K vacuum chamber using a mechanically stable support with low heat conductance. The maximum temperature difference along the heat shield is less than 6 K, which ensures low radiative load to the 4 K stage located inside the 77 K thermal shield. The 4 K

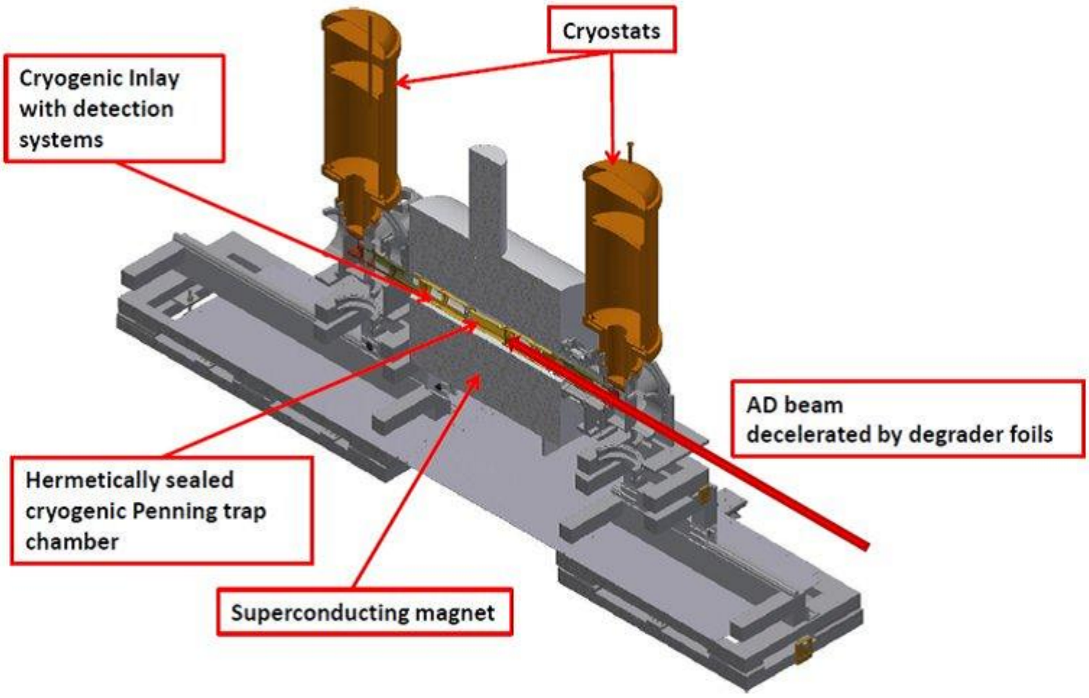

Fig. 3.1: Experimental apparatus consists of a superconducting magnet, cryostats, electronics interfaces, and the Penning trap stack. The whole apparatus will be housed in a temperature stabilized Faraday cage.

stage includes the sealed vacuum chamber with the Penning trap can inside, the detection electronics, and a support structure, which will be thermally anchored to the liquid helium baths of the cryostats. Two annealed high-purity copper rods with a diameter of 16 mm and a thermal conductivity of 1000 W/m K at 4.2 K will be used for the heat transport. Since the 4 K stage is attached on both ends to the liquid helium reservoirs of the cryostats, the total heat load to the 4 K stage is low.

At the upstream part of the trap can, the degrader is placed to reduce the antiproton energy from the Antiproton Decelerator (AD) of CERN. Transmitted antiprotons have lost energy due to electromagnetic interaction with the degrader material, which is described by a modified Bethe Bloch formula [24]. In the downstream part of the trap can, detection electronics are connected to the trap via the pinbase. The details of the electronic chamber is discussed in section 4.3.1. Filter boards are mounted to the downstream part of the electronic chamber for the purpose of filtering RF noises of the DC voltage which is supplied from the room temperature electronics.

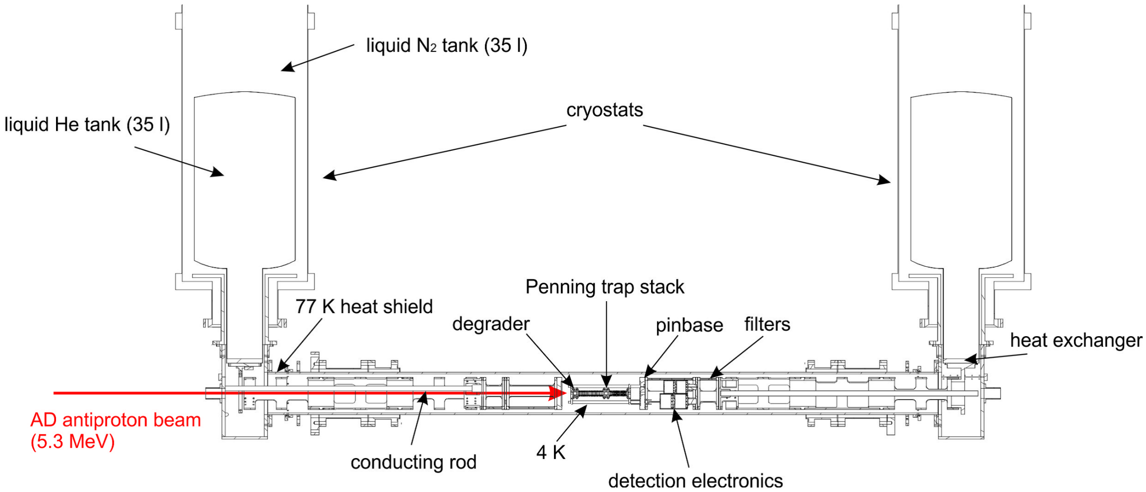

Fig. 3.2: Illustration of a cross section of the apparatus. Inner part of the apparatus is maintained 4 K environment and is surrounded by a 77 K thermal shield. In practice, the Penning trap stack is contained inside the trap can, which is not shown in the figure.

§ 3.2 Cylindrical Penning trap stack

The trap system is shown in Fig. 3.3 and consists of four stacked cylindrical Penning traps. All traps are in a cylindrical five-pole, orthogonal, and compensated design [25]. Such a five-pole trap consists of two end-cap electrodes, two correction electrodes and the central ring electrode. Features of each traps are described in below.

- Catching trap (CT): The degraded antiprotons will be accumulated here. It will be used as reservoir of antiprotons and single particles will be prepared from the CT to transfer to the other traps.
- Precision trap (PT): Measurement of the cyclotron frequency ω_c and the Larmor frequency will take place here.
- Analysis trap (AT): The magnetic bottle is superimposed to this trap to determine the spin eigen-state.
- Monitor trap (MT): It will be used for efficient cooling of the cyclotron motion of an antiproton. In a first attempt a single monitor-antiproton will be stored in the trap which will be used for permanent magnetic field monitoring. The necessity of cooling the cyclotron motion is discussed in section 4.5.

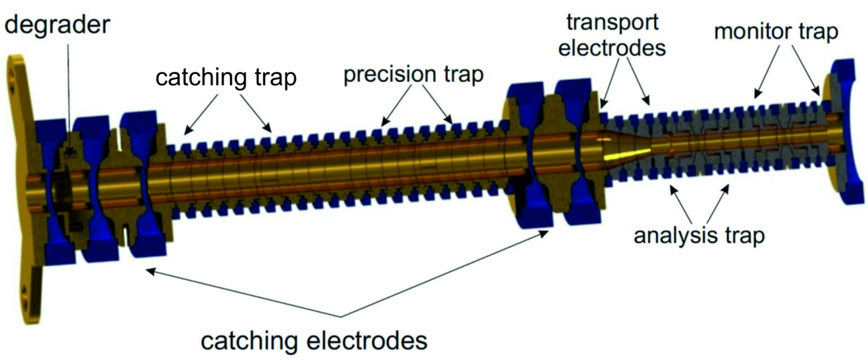

Fig. 3.3: Schematic of the Penning trap stack. It consists of four cylindrical Penning traps. Refer to the text for the details.

Catching electrodes are used for catching the low evergy tail of the degraded antiproton beam. They will be operated in relatively high voltages (∼15 kV). The upstream catching electrode will be pulsed from 0 V to 15 kV after the antiprotons have passed. In this way, the antiprotons can be confined between the catching electrodes and cooled below 100 meV by electron cooling [26] into the harmonic potential well of the CT.

Chapter 4

Detection System

A single particle stored in a cryogenic Penning trap has three eigen-motions; the modified cyclotron motion, the magnetron motion, and the axial motion (for the details, see section 2.1). Information of these motions can be extracted by the detection of image currents, which are induced in the trap electrodes caused by the oscillating particle [27][28][29]. However, it requires one's ingenuity, since these currents are only in the order of fA. Thus, highly sensitive detection systems which consist of a resonator with high quality factor (Q-value) and an ultra-low noise amplifier are utilized. These detection systems are the only way to acquire frequency information from the stored particle. This makes them a key component of the experiment. A high sensitivity of the detection system leads to fast measurement cycles. This reduces systematic effects of the measured results, which is important to measure the g-factor accurately. In this chapter, the principle and development of the detection system are presented.

§ 4.1 Principle of a single particle detection system

In a Penning trap the eigen-motions of a particle induces tiny image currents in the electrodes, which can be detected. To this end, an inductor and an ultra-low noise amplifier are connected to one of the Penning trap electrodes. Fig. 4.1(a) shows a schematic of a Penning trap and a detection system. Since a Penning trap is made out of a stack of electrodes, it has a parasitic capacitance C_T, therefore, Fig. 4.1(a) can be converted to a schematic as it is shown in Fig. 4.1(b), where I is the image current.

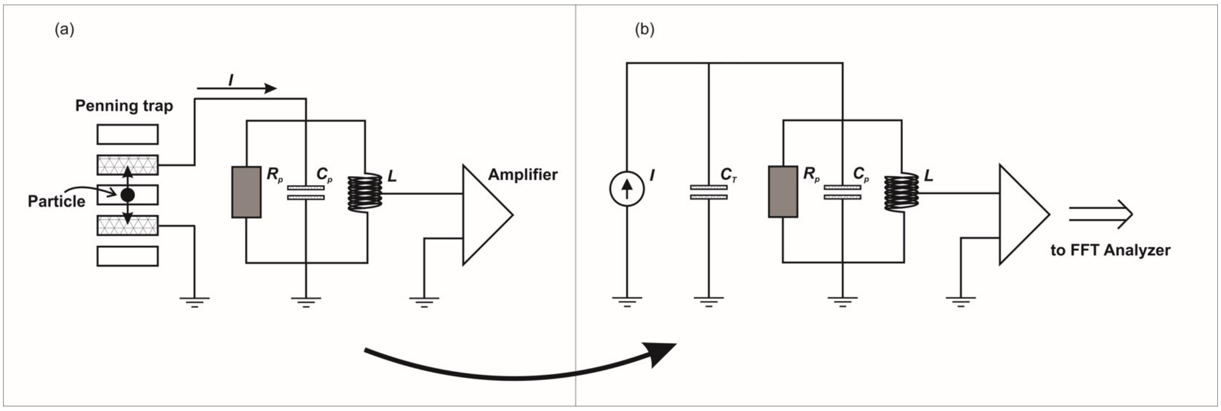

Fig. 4.1: (a) Schematic of a Penning trap and a detection system. (b) Considering that a Penning trap is made out of a stack of electrodes, it can be converted to such a schematic.

From now on, the determination of the equivalent circuit of an inductor (as shown in Fig. 4.1) will be explained. In reality, an inductor has not only an inductance L, but it also has two additional ingredients; a parasitic series capacitance C_s and parasitic series resistance R_s (Fig. 4.2). C_s is a capacitance due to a capacitance between wires of the inductor C_W and a capacitance between wires and the housing C_H. It is obvious that an inductor has also a parasitic resistance R_s since it is made out of a metal wire.

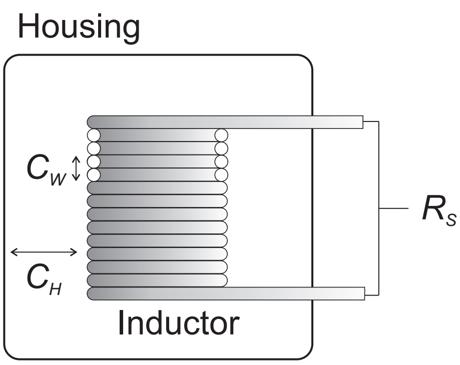

Fig. 4.2: Schematic of an inductor. In reality, it has a parasitic capacitance C_s and a parasitic series resistance R_s, in addition to an inductance L. C_s includes a capacitance between wires C_W and a capacitance between wires and the housing C_H.

Therefore, an inductor can be considered as a series tuned circuit as in Fig. 4.3.

A quality of inductors is often defined by the Q-value, which is a ratio of stored energy E to an energy loss per one oscillation cycle.

$$Q = 2\pi \cdot \frac{E}{\Delta E} \tag{4.1}$$

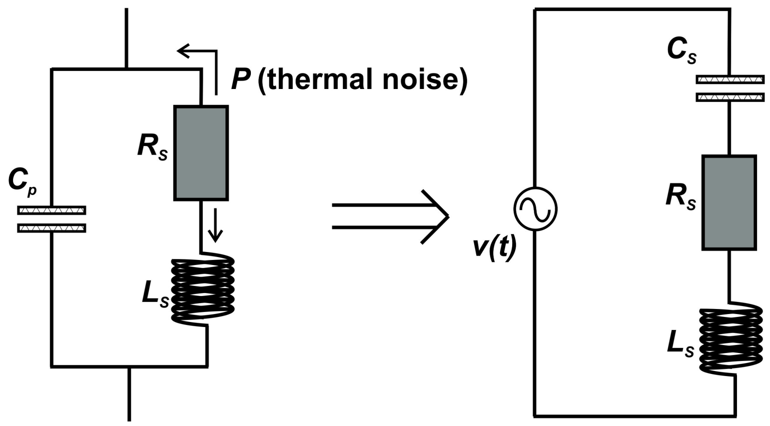

Fig. 4.3: Left: Equivalent circuit of an inductor. The parasitic series resistance R_s generates a thermal noise P. Therefore, it can be consider as a series tuned circuit as in the right figure.

Considering the Q value for the series tuned circuit Q_s, it can be written as:

$$Q_s = 2\pi \cdot \frac{\int v(t)i(t)dt}{R_s I_{rms}^2 T_s} = \omega_s \cdot \frac{L_s I_{rms}^2}{R_s I_{rms}^2} = \frac{\omega_s L_s}{R_s} = \Big(\frac{1}{\omega_s C_s R_s}\Big), \tag{4.2}$$

where ω_s is the resonance frequency of the series tuned circuit. In addition, the impedance of the circuit Z_s is;

$$Z_s = R_s + j\omega L_s + \frac{1}{j\omega C_s}. \tag{4.3}$$

These equations are needed for considering the conversion of the series tuned circuit to the parallel tuned circuit. Now, because the admittance of the parallel tuned circuit Y_p can be written as in equation (4.4), and comparing it with equation (4.3), there is a duality between these two circuits. The duality is shown in Table 4.1.

$$Y_p = \frac{1}{R_p} + j\omega C_p + \frac{1}{j\omega L_p} \tag{4.4}$$

Thus, by using this relationship as in Table 4.1, the equivalent series circuit can be converted to the parallel circuit as shown in Fig. 4.4. In addition, the Q-value for the parallel tuned circuit Q_p can be written as equation (4.5) by using equation (4.2) and Table 4.1:

$$Q_p = \frac{1}{\omega_p L_p \frac{1}{R_p}} = \frac{R_p}{\omega_p L_p}, \tag{4.5}$$

where ω_p is the resonance frequency of the parallel tuned circuit. Considering the fact that the heat dissipation has to be identical between these two circuits, Q_s and Q_p must

Series tuned circuit	Parallel tuned circuit
Voltage source	Current source
I	V
R_s	$1/R_p$
L_s	C_p
C_s	L_p
Z_s	Y_p

Table 4.1: Duality between series and parallel tuned circuit

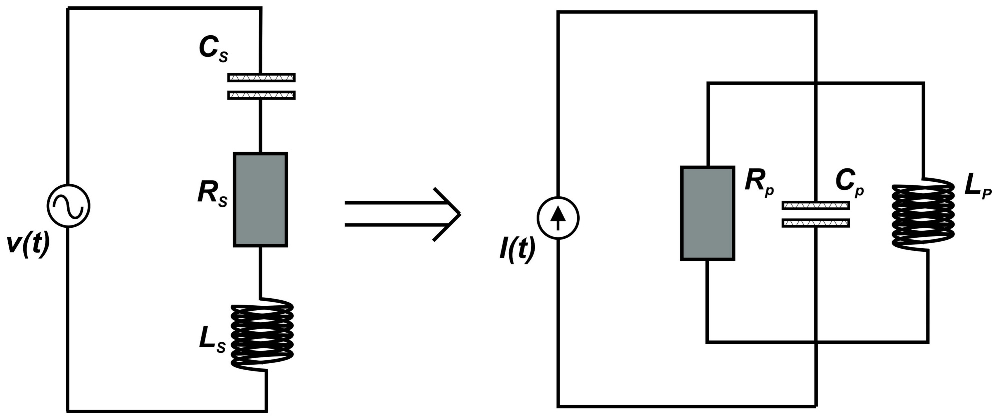

Fig. 4.4: Conversion of the series tuned circuit to the parallel tuned circuit using the duality as shown in Table 4.1.

be the same. Moreover, ω_s and ω_p must be equal so as to have a same resonance frequency between these two circuits. From equations (4.2) and (4.5), together with the fact that the resonance frequency can be represented as $\omega_x = 1/\sqrt{L_x C_x}$, relation of the parameters can be written as:

$$L_s = L_p = L \tag{4.6}$$

$$C_s = C_p \tag{4.7}$$

$$\omega_s = \omega_p = \omega_0 \tag{4.8}$$

$$Q = \frac{\omega_0 L}{R_s} = \frac{R_p}{\omega_0 L}. \tag{4.9}$$

Therefore, from this argument, the equivalent circuit of an inductor can be represented as shown in Fig. 4.1.

Going back to the subject, by connecting an inductor to a Penning trap, it forms a tuned circuit with its resonance frequency:

$$\omega_0 = \sqrt{\frac{1}{L(C_p + C_T)}}. \tag{4.10}$$

In addition, from equations (4.9) and (4.10), the effective parallel resistance R_p can be expressed as:

$$R_p = \omega_0 L Q. \tag{4.11}$$

To think about detection of image currents and sensitivity of the detection system, it is also useful to consider an equivalent circuit of the input part of the amplifier. Fig. 4.5 shows such a circuit of the detection system together with a Penning trap.

The input part of the amplifier has a parasitic capacitance C_{amp} and an input resistance R_{amp}. Neglecting a change of the resonance frequency ω_0 by connecting the amplifier, and by tuning ω_0 to the frequency of the eigen-motion of a particle ω_p or vice versa, a voltage drop $V = R_{eff} I$ at the motional eigen frequency of the particle occurs across the detector, where R_{eff} is the effective parallel resistance of the whole detection system. This voltage drop is amplified and a frequency spectrum will be obtained by a FFT analyzer. The sensitivity of the detection system is strongly related to R_{eff}, and it is necessary to make it large as possible (this will be discussed in section 4.2.2). Since R_{eff} is the parallel resistance of R_p and R_{amp}, these resistances should be large as well. As R_p can be expressed as in equation (4.11), the inductance L and the quality factor Q should be as

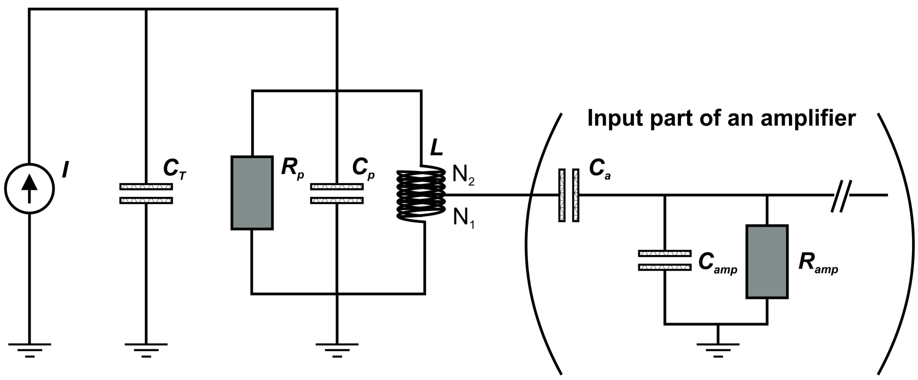

Fig. 4.5: Equivalent circuit of an amplifier together with the equivalent circuit of a resonator and a Penning trap.

large as possible under given experimental constraints. Regarding to make R_{amp} large, it is necessary to consider the type of transistors which are used, type of material for the board, etc.

§ 4.2 Dip detection

To measure the axial frequency of a particle, the so called *dip detection* is utilized. In this section, the principle of this method is described.

§ 4.2.1 Equation of the axial motion

The axial motion of a particle stored in a Penning trap can be considered as a damped harmonic oscillator, because the amplitude of the oscillation of a particle decreases via the resistive cooling due to the thermal contact between the detector resistance R_{eff}. Thus, the equation of the axial motion can be written as:

$$m\frac{d^2z}{dt^2} = -m\left(\gamma\frac{dz}{dt} + \omega_z^2 z\right) \tag{4.12}$$

Where z is the axial coordinate, γ the damping constant, and ω_z the axial frequency, respectively. By multiplying this equation by dz/dt and time-integrating the result, the equation below is obtained.

$$\frac{1}{2}m\left(\frac{dz}{dt}\right)^2 + \frac{1}{2}m\omega_z^2 z^2 = -\int m\gamma\left(\frac{dz}{dt}\right)^2 dt = -\int P dt \tag{4.13}$$

P is the power dissipation due to the image current flowing through R_{eff}. From the equation above,

$$P = R_{eff} I^2 = m\gamma \frac{d^2 z}{dt^2} \tag{4.14}$$

is derived, and also by solving for γ,

$$\gamma = \frac{R_{eff} I^2}{m(\frac{dz}{dt})^2} \tag{4.15}$$

is obtained. Together with the equation of the image current $I = \frac{q}{D}\frac{dz}{dt}$($q$ is the charge, D the effective electrode distance. For the big Penning traps, such as the Catching trap and the Analysis trap, $D = 10$ mm), equation (4.15) can be rewritten as:

$$\gamma = \frac{R_{eff}}{m}\frac{q^2}{D^2} \iff \tau = \frac{m}{R_{eff}}\frac{D^2}{q^2} \tag{4.16}$$

τ is called *the cooling time constant*, which defines the amount of time needed for a particle to cool down to a fraction 1/e of the initial energy. By combining equations (4.12) and (4.16),

$$m\frac{D^2}{q^2}\frac{d}{dt}I + R_{eff}I + m\omega_z^2 \int \frac{D^2}{q^2} I dt = 0 \tag{4.17}$$

is obtained. By replacing $l = m\frac{D^2}{q^2}$ and $c_p = \frac{1}{m\omega_z^2}\frac{q^2}{D^2}$, the equation above represents a series tuned circuit:

$$l\frac{d}{dt}I + R_{eff}I + \frac{1}{c_p}\int I dt = 0. \tag{4.18}$$

The reactance of a series tuned circuit is zero on resonance. Thus, when tuning the resonance frequency to the axial motion of the particle, the particle shorts the effective parallel resistance of the whole detection system. This means that when the particle frequency is identical to the resonance frequency of the detector, the particle shorts the thermal noise of the detector which causes a dip in the frequency spectrum (Fig. 4.6) [30].

The dip center is determined by performing a non-linear least-squares fit. The expected frequency scatter σ obtained from the least-squares fit can be evaluated [31], with the result:

$$\sigma \approx \sqrt{\frac{11}{9}}\sqrt{\frac{1}{4\pi}\frac{\Delta\nu}{T_{avg}}\frac{1}{\mathrm{SNR}}}, \tag{4.19}$$

where $\Delta\nu$ is the width of the dip, T_{avg} the averaging time, and SNR the signal-to-noise-ratio. To obtain a low frequency scatter in a defined averaging time, SNR needs to be large and $\Delta\nu$ small. However, $\Delta\nu$ can not be smaller than σ, otherwise the dip can not be resolved.

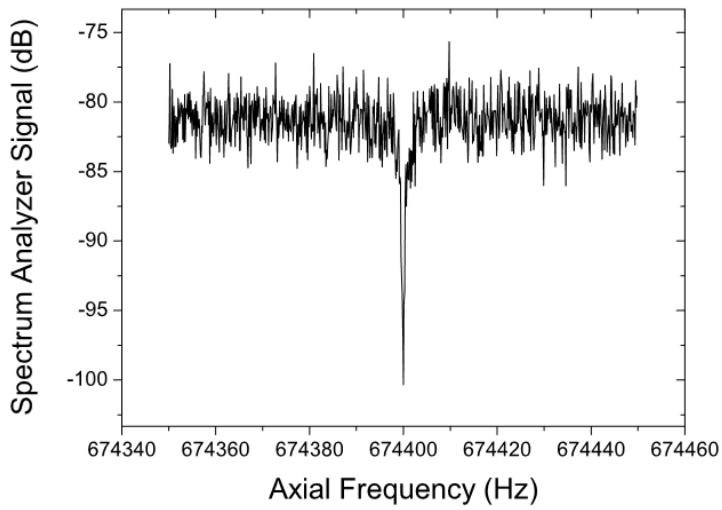

Fig. 4.6: Example of a dip of the frequency spectrum from the BASE collaboration at the University of Mainz. The data shows a frequency dip at the axial frequency of a single proton in a Penning trap.

§ 4.2.2 Optimizing the dip detection of the axial detectors

As a large SNR reduces the frequency scatter, it is an important goal in the development of image current detection systems to maximize the SNR. In case of dip detection, SNR is defined by the ratio of the Johnson-Nyquist noise of the tank circuit u_n [nV/$\sqrt{\text{Hz}}$] to an equivalent input noise of the amplifier e_n [nV/$\sqrt{\text{Hz}}$] [32][33]:

$$u_n = \sqrt{4k_BTR_{eff}} \cdot \kappa \tag{4.20}$$

$$\text{SNR} = \frac{u_n}{e_n} = \frac{\sqrt{4k_BTR_{eff}} \cdot \kappa}{e_n}, \tag{4.21}$$

where k_B is the Boltzmann-constant, T the temperature of the detector, κ the coupling constant, and e_n the equivalent input noise of the amplifier, respectively. The coupling constant is a multiplication of *the coupling constant of the capacitance* κ_c and *the coupling constant of the inductor* κ_l. κ_c is a function of capacitance of the capacitor C_a and the input capacitance of the amplifier C_{amp}. On the other hand, κ_l is defined by a ratio of the length of the inductor N_1 and N_2 (see Fig. 4.5).

$$\kappa = \kappa_c \cdot \kappa_l = \frac{C_a}{C_a + C_{amp}} \cdot \frac{N_1}{N_1 + N_2} \tag{4.22}$$

From equation (4.21), one might jump to conclusion at first glance that maximizing κ is a solution for maximizing the SNR, however in reality it is not so simple. R_{eff} is also a function of κ, which monotonically decreases while κ is increased (Fig. 4.7(a)):

$$R_{eff} = \frac{R_p R_{amp}/\kappa^2}{R_p + R_{amp}/\kappa^2}. \tag{4.23}$$

As described previously, the sensitivity of the detection system is strongly related to R_{eff}. One of the reason is that the full width at half maximum of the particle dip $\Delta\nu$ is proportional to R_{eff}:

$$\Delta\nu = \frac{1}{2\pi}\frac{1}{\tau} = \frac{1}{2\pi}\frac{R_{eff}}{m}\frac{q^2}{D^2}. \tag{4.24}$$

The smaller R_{eff} is, the smaller $\Delta\nu$ will be. One of the major problem of small $\Delta\nu$ is that it makes it necessary to average the obtained frequency spectrum over many times until it gets to required frequency resolution. This leads to make the measurement cycle longer, thus the larger the affect from external drifts. Therefore, it is not a simple case as just to consider maximizing the SNR (Fig. 4.7(b)), the relationship of $\Delta\nu$ and κ must also be taken into account (equation (4.24)).

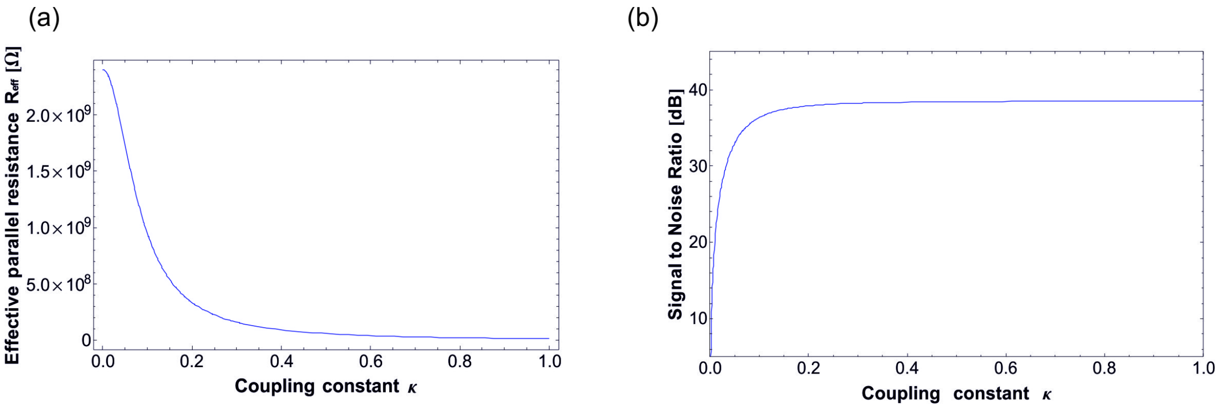

Fig. 4.7: (a) Example of a graph of the effective parallel resistance R_{eff} as a function of the coupling constant κ. R_{eff} decreases while κ increases. (b) Example of a graph of the SNR as a function of the coupling constant κ. The sensitivity of the detection system is strongly related to R_{eff} ($\propto \Delta\nu$), thus it is not a simple case as just to increase κ so as to increase the SNR. Considering the relation between $\Delta\nu$ and κ must be also taken into account.

§ 4.3 Development of the resonator

The resonators are placed as close as possible to the Penning trap system. The smaller the length of the connection leads the smaller resistive losses and stray capacitances. This increases the Q-value of the detectors, and thus sensitivity. Two big axial resonators for the PT and AT, two small axial resonators for the CT and MT, and two cyclotron resonators will be mounted inside the electronics chamber (Fig. 4.8), which is located downstream to the trap can. Two cyclotron resonators are provided for the PT and MT. The geometry of the resonators is determined by the geometrical constraints of the chamber.

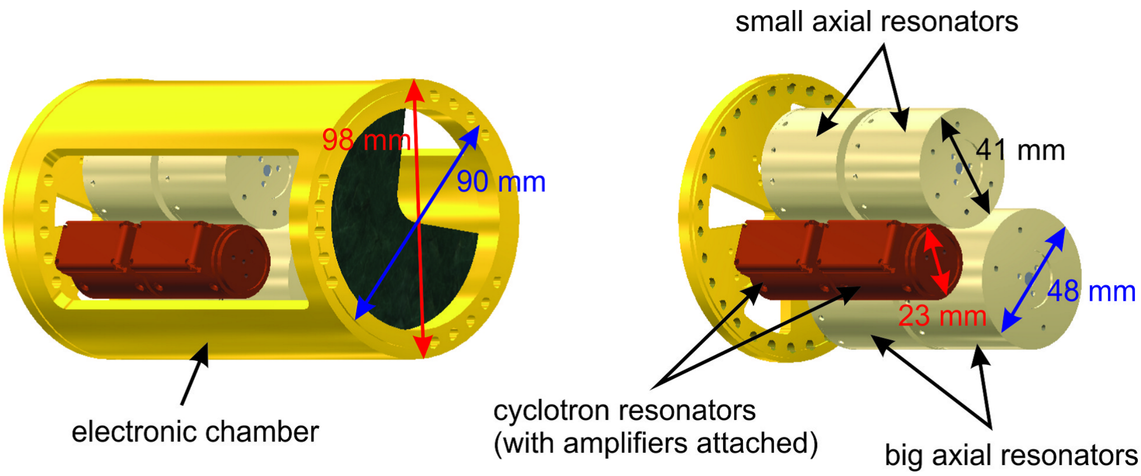

Fig. 4.8: Illustration of the electronic chamber and the resonators. Two big axial resonators, two small axial resonators, and two cyclotron resonators will be mounted inside the chamber. The two big axial resonators are provided for the PT and the AT, whereas the two small ones are provided for the MT and the CT. The two cyclotron resonators are applied for the AT and the PT. The cyclotron resonators will be used for the resistive cooling of the cyclotron motion of a particle stored in a Penning trap. This will be discussed in section 4.5.

All axial resonators are made out of a superconducting toroid in a metal shielding. The magnetic field flux of a toroid is totally contained inside the toroid, which prevents eddy current losses in the housing. The metal shield has a diameter of 48 mm for the big axial ones, and 41 mm for the small axial ones (refer to Fig. 4.8). The geometry of the toroid was optimized in a way, that the cross sectional area is maximized at the lowest length of a superconducting wire. For the superconducting wire, polytetrafluoroethylene

(PTFE) insulated NbTi wire of $2r$ =75 μm is utilized. NbTi is a type II superconductor with a high critical magnetic field strength of B_{c2}=14.5 T. This enables to place the detectors close to the trap system, which is mounted in the high magnetic field of the superconducting magnet (B_0=1.9 T). The windings are fixed to the core by PTFE thread seal tape to ensure a good heat contact between the wire and the PTFE core. This is because at the phase transition to the superconducting state, electrons condense to the BCS ground state which leads to a decrease in the heat conduction coefficient of NbTi [34]. Fig. 4.9 shows a sketch of the small axial resonator.

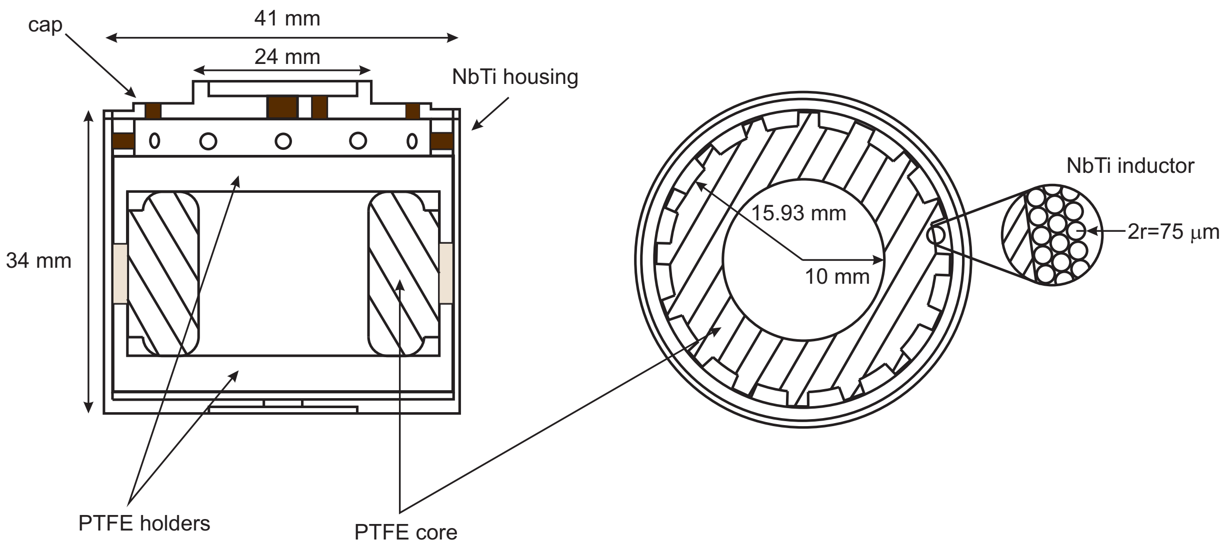

Fig. 4.9: Sketch of the small axial superconducting resonator. The toroid core is made out of PTFE, and PTFE insulated NbTi superconducting wire is used for the windings. The toroid is mounted inside the NbTi housing and kept stable with the PTFE holder. It is enclosed by putting the cap from outside.

§ 4.4 Principle of the amplifier for the axial detection system

The amplifier for the axial detection system requires several different features: a low equivalent input noise e_n and a high equivalent input resistance R_{amp}. In this section, the design and the development of the ultra-low noise amplifier are described.

§ 4.4.1 Metal Semiconductor Field Effect Transistor (MES-FET)

A transistor can be used to amplify electronic signals, so it is one of the main components of an amplifier. In the BASE project, Metal Semiconductor Field Effect Transistors (MES-FET) are used for all of the amplifiers (Fig. 4.10).

The gate electrode and the semiconductor of MES-FETs form a Schottky junction. This distinguishes them from J-FETs and MOS-FETs, which have a p-n junction at the gate. GaAs is used as a semiconductor for most of MES-FETs, whereas Si is applied for most of J-FETs and MOS-FETs. In particular, GaAs MES-FET are used, since they work under cryogenic conditions due to the small band-gap of GaAs [35][36][37].

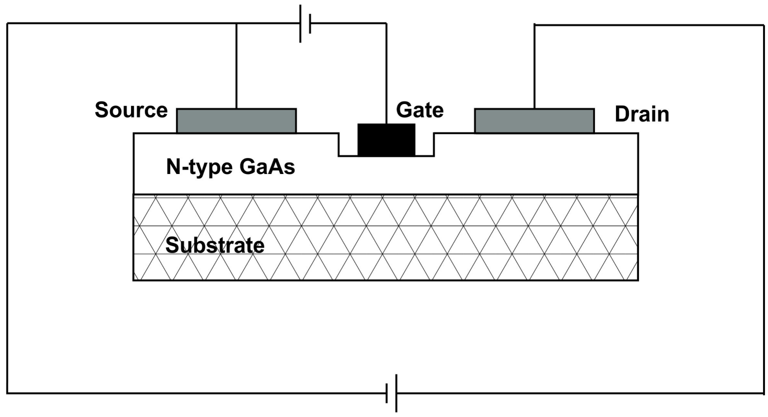

Fig. 4.10: Schematic of a MES-FET. The gate electrode and the semiconductor form a Schottky junction. When the gate is negatively biased, it forms a depletion layer underneath the gate electrode, which decreases the current flow. Therefore, the current flow can be controlled by varying the gate bias voltages. In that sense, it behaves like a voltage controlled resistor with a large transconductance. The gate can not be operated with positive voltages, since electrons will flow into the gate from the semiconductor.

When the gate bias voltage is 0 and the drain is biased, a current will flow from drain to source. When a negative voltage is applied to the gate, the depletion layer of the Schottky junction increases, which decreases the drain current. In that sense, a MES-FET behaves like a voltage controlled resistor with large transconductance. Therefore, the drain current can be controlled by varying the gate bias voltages.

§ 4.4.2 Basic circuits

As described in the previous subsection, the drain current can be controlled by the gate bias voltages. Moreover, by putting a resistor to an appropriate position of a circuit, a voltage signal is obtained. In principle, the position of the resistor defines the characteristic of a transistor circuit. For our purpose, a common-source FET circuit and a source-follower FET circuit are utilized. In Fig. 4.11, the basic circuit of those two configuration are shown.

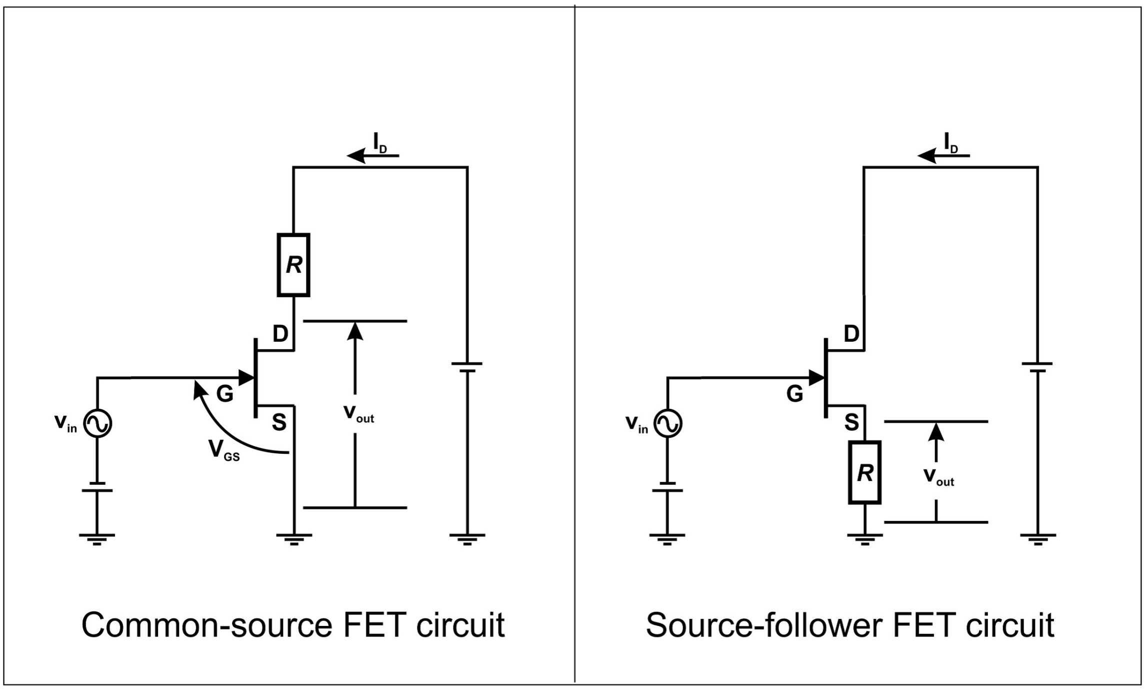

Fig. 4.11: Left: Schematic of a common-source FET circuit. It has a high input impedance and provides a high gain. Right: Schematic of a source-follower FET circuit. It has a low output impedance and enables the impedance matching to the FFT analyzer.

A common-source circuit has a high input impedance and provides a high gain. Since the signal induced by the interaction between a particle and the electrodes of a Penning trap is in the order of fA, these features are essential. However, the output impedance of a common-source circuit is relatively high and it is not suited for the impedance matching to the FFT analyzer (50 Ω input impedance). Compared to that, a source-follower has a low output impedance, which can be used for impedance matching, but it has no gain. By combining these two circuits properly, it is possible to obtain an amplifier for our experiment.

§ 4.4.3 Common-source FET circuit

As mentioned previously, the gate bias voltages of a N-channel MES-FET can only be operated in negative voltages. To see how the drain current I_D varies with the gate bias voltages V_{GS}, an example of the I_D vs V_{GS} curve (I-V curve) of a common-source circuit is shown in Fig. 4.12.

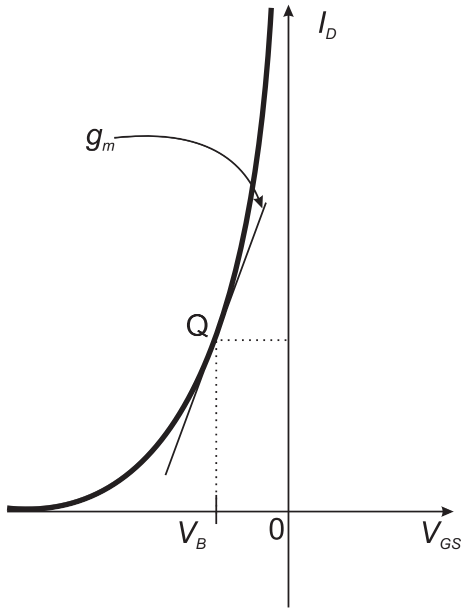

Fig. 4.12: Example of an I-V curve of a common-source N-channel MES-FET circuit. When the amplitude of the input voltage signal v_{in} is small enough, it can be considered as a straight line at the point Q. The slope g_m (transconductance) of the line relates the input signal v_{in} to the output signal v_{out} ($v_{out} = -Rg_m v_{in}$).

It is always necessary to apply the bias voltage so as to make all part of the input signal are in the negative voltage region. Otherwise, the shape of the amplified signal would not be similar to the input signal. Note that this principle only holds while operating N-channel MES-FET.

Assume that the applying gate bias voltage is V_B, and the amplitude of the input voltage signal v_{in} is small enough that the curve can be considered as a straight line at the point Q (see Fig. 4.12). The slope g_m of the line is called the transconductance. On this condition, the drain current i_D can be written as a simple multiplication of v_{in} and g_m; $i_D = g_m v_{in}$. Therefore, the output signal v_{out} can be written as; $v_{out} = -Rg_m v_{in}$. The minus sign must be included since v_{out} has an opposite phase compared to v_{in}. Thus, the voltage gain A is yielded:

$$A = -Rg_m. \tag{4.25}$$

The input impedance of a transistor is an important parameter to be considered, since it is one of the main factor which defines the input resistance of the amplifier R_{amp}. The gate of a common-source FET circuit has almost no current when the voltage is applied to the gate electrode. Therefore, it indicates that there is no resistive ingredient at the gate, thus the input impedance of the circuit is infinite, ideally. This is one of the reasons why these FETs are utilized for our experiment. However, it is not suited for connecting it directly to external devices, since the output impedance of this circuit is quite large. Typically, the input impedance of the spectrum analyzer is 50 Ω and it is much smaller than the output impedance of a common-source circuit. Therefore, when the amplified signal is detected by the analyzer, most of its power is lost due to the impedance mismatching. This problem can be solved by connecting a source-follower circuit to the output.

§ 4.4.4 Source-follower FET circuit

A source-follower circuit is one of the general FET circuits which has its drain AC-wise grounded (common-drain). A low output impedance makes it possible utilize this circuit as an impedance matching device. To calculate the output impedance, an equivalent circuit of a source-follower should be considered (Fig. 4.13).

The output impedance can be calculated as follows; applying no signal to the input, and applying a voltage signal to the output instead. Fig. 4.13 can be modified for the purpose of calculating the output impedance (Fig. 4.14).

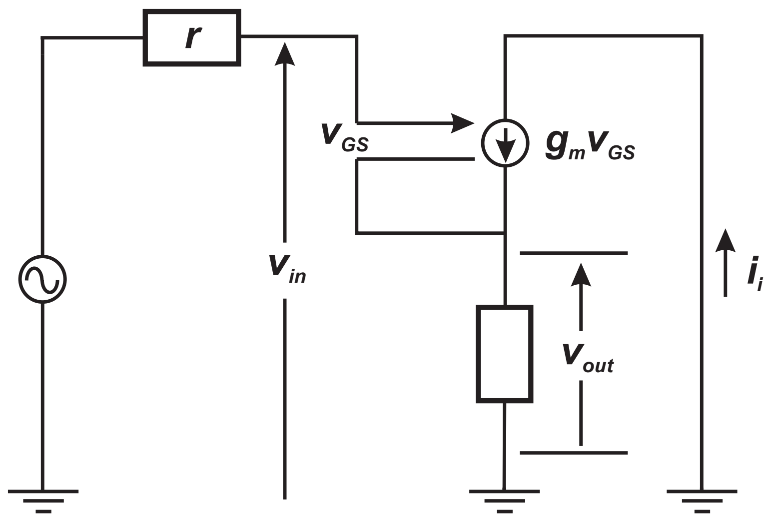

Fig. 4.13: Equivalent circuit of a source-follower circuit.

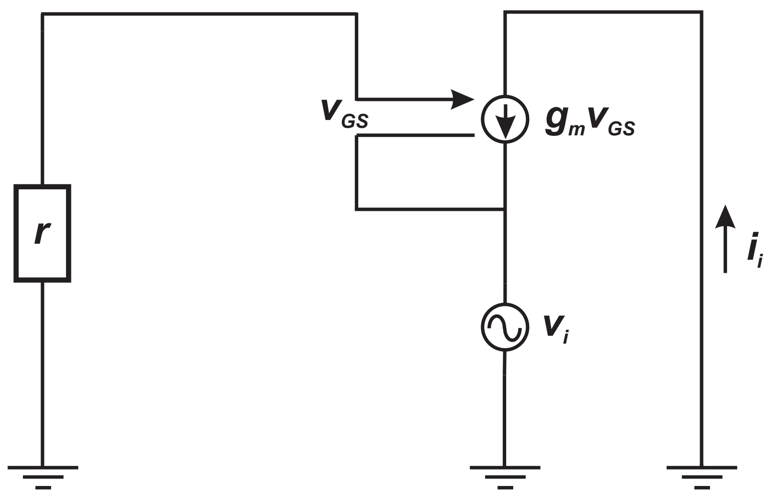

Fig. 4.14: Equivalent circuit of a source-follower circuit for the calculation of its output impedance. It can be calculated by applying no signal to the input, and applying a voltage signal to the output. From equation (4.26), the output impedance R_{out} of the source-follower is very small compared to that of the common-source. This leads to achieve the impedance matching to the FFT analyzer.

From Fig. 4.14, the output impedance of the source-follower circuit is obtained:

$$R_{out} = \frac{v_i}{i_i} = \frac{v_i}{-g_m v_{GS}} = \frac{v_i}{-g_m(-v_i)} = \frac{1}{g_m}. \tag{4.26}$$

Therefore, the output impedance of a source-follower circuit is much smaller compared to a common-source circuit, and this enables the impedance matching with a spectrum analyzer. Likewise, the input impedance of a source-follower circuit is infinite. This ensures that the amplified signal has almost no losses when it passed through the input of a source-follower circuit.

§ 4.4.5 The ultra-low noise amplifier

In the previous subsections, basics of a common-source and a source-follower circuit are described. The next step is to combine these circuits together and make it for practical use. Aiming for designing the amplifier which has extremely low noise, it is not so simple as just to connect these two circuits in series. First, low pass filters must be included for all bias voltages for the purpose of attenuating RF noises and bypassing the DC voltages. A first-order low pass filter consists of a resistor and a capacitor as shown in Fig. 4.15.

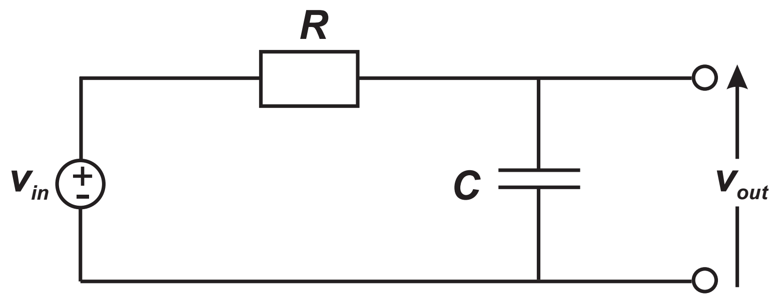

Fig. 4.15: Schematic of the basic low pass filter circuit. It is mainly used for attenuating RF noises and bypassing the DC voltages.

Ignoring the phase and only considering the amplitude, the output voltage signal v_{out} can be written as:

$$v_{out} = \frac{1}{\sqrt{4\pi^2\nu^2R^2C^2+1}} \cdot v_{in}, \tag{4.27}$$

where ν is the frequency of an input signal, R the resistance, and C the capacitance, respectively. Equation (4.27) indicates that the output voltage v_{out} decreases while the frequency ν is increased. The cutoff frequency ν_{cf} is defined by:

$$\nu_{cf} = \frac{v_{out}}{v_{in}} \times \frac{1}{\sqrt{2}}. \tag{4.28}$$

ν_{cf} is adjusted in a way to be suited for each purposes.

In section 4.2.2, the importance of making R_{amp} large is described, and the strong relation between the input impedance of the FET circuit is discussed in section 4.4.3. Another factor to make R_{amp} large is to consider the type of material for the circuit board. It is also important to utilize materials with small loss tangent δ in order to minimize the dissipation due to polarization in the insulators.

Up to this point, mostly the optimization of R_{amp} has been mentioned. In addition, it is necessary to consider the equivalent input noise of the amplifier e_n. e_n is mostly defined by the 1/f noise and the thermal noise of the FET. The characteristic of the noise is completely determined by manufacturing processes of the FETs, and in principle the noise characteristics in the low frequency range used at BASE (ν_z ~600 to 800 kHz, ν_c ~28.9 MHz) are not included in the specifications, since GaAs FETs are usually designed for fast switching applications (ν >100 MHz). Therefore, the only solution to make e_n small is to test many kinds of FETs.

§ 4.5 Feedback cooling using the cyclotron detection system

Decreasing the energy of the antiproton stored in a cryogenic Penning trap leads to decrease the line width of the cyclotron resonance and the Larmor resonance. Eventually, it leads to increase the experimental precision. By using the so-called feedback cooling technique, one can manipulate antiproton temperature by controlled feedback. The schematic of the technique is presented in Fig. 4.16. The detector is represented by the effective parallel resistance R_{eff} in series to a thermal noise e_{th}. The ultra-low noise amplifier is represented with the equivalent input noise e_n. The signals are picked up, amplified and fed back to the trap via a splitter, phase shifter, and a voltage controlled attenuator. The feedback gain G_{FB} can be adjusted by the voltage controlled attenuator.

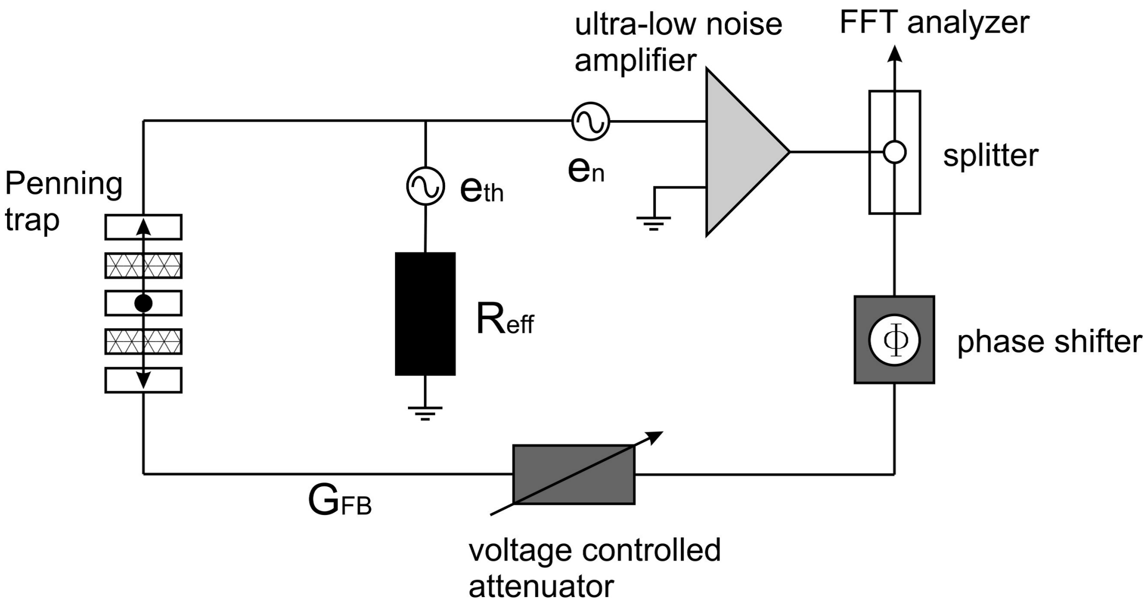

Fig. 4.16: Experimental schematic of the feedback technique. The detector is represented by the effective parallel resistance R_{eff} in series to a thermal noise e_{th}. The ultra-low noise ampliifer is represented with the equivalent input noise e_n. The voltage drop occurred at the resistor is amplified and fed back to the trap via a splitter, phase shifter, and a voltage controlled attenuator.

Considering the voltage drop V_p occurred when the particle current I_p flows through the resistor R_{eff}, the feedback signal manipulates the particle motion as presented in Fig. 4.17. The signal is instantaneously fed-back to the particle with feedback-gain G_{FB}.

Seen from the particle, the effect of G_{FB} looks like a resistor with modified absolute value R'_{eff}.

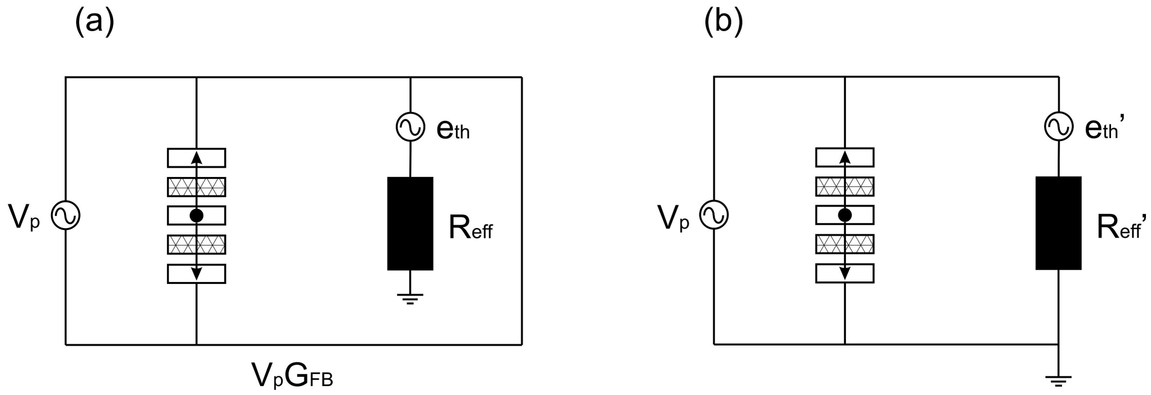

Fig. 4.17: (a) Feedback technique applied to a particle in a Penning trap. The detector signal is fed-back to the particle with a feedback gain G_{FB}. (b) Modified absolute value R'_{eff} due to the feedback when it has seen from the particle.

Taking into account that V_p is identical to V'_p, the relation to these effective values are evaluated:

$$V_p = I_p R_{eff} \pm G_{FB} I_p R_{eff} \tag{4.29}$$

$$V'_p = I_p R'_{eff} \tag{4.30}$$

$$R'_{eff} = R_{eff}(1 \pm G_{FB}). \tag{4.31}$$

Equation (4.31) is derived by equating equations (4.29) and (4.30). The effective temperature T_{eff} is derived by the same argument as for the case of the resistors, and it can be written as:

$$T_{eff} = T_0(1 \pm G_{FB}), \tag{4.32}$$

where T_0 is the temperature of the detection system. From equation (4.32), the application of the feedback affects the temperature of the particle. Negative feedback [38] reduces its temperature, whereas the positive feedback increases, respectively.

The feedback device which is expected to utilize for manipulating the cyclotron motion is under development. Efficient cooling of the cyclotron mode is crucial for the spin flip experiment. In practice, not only the spin of a particle couples to the magnetic bottle at the AT, but also the cyclotron energy also couples as well. A cyclotron quantum transition shifts the axial frequency by 63 mHz, which leads to axial frequency fluctuations. This eventually limits the detectability of the spin state. The rate of the quantum jump is low while the cyclotron energy is low [39][40]. Therefore, aiming for a good resolution of the antiproton spin-state, efficient cooling of the cyclotron motion is an extremely important issue. In Fig. 4.18, it shows photographs of the cyclotron feedback cooling devices.

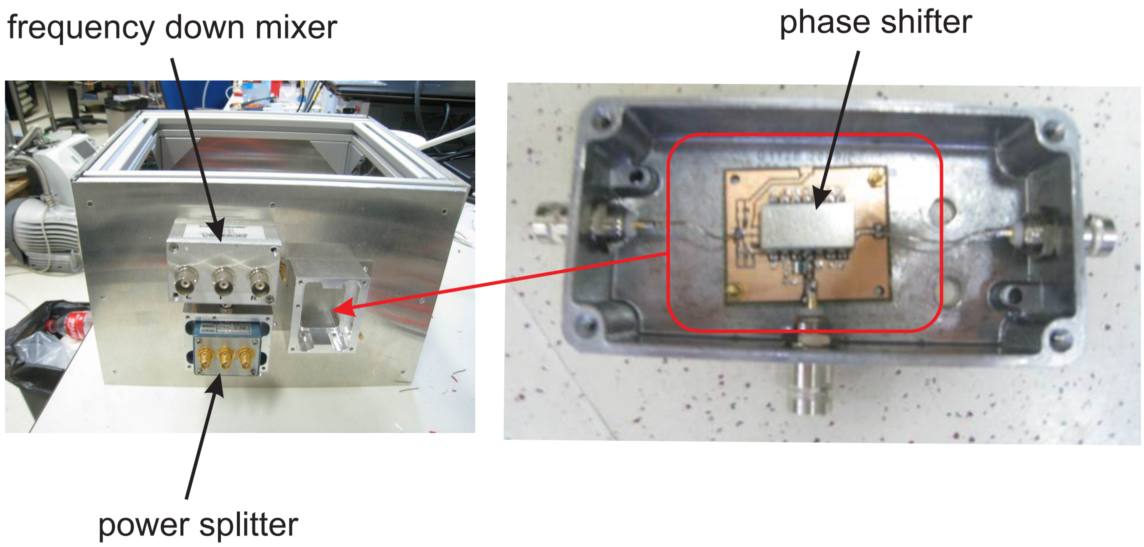

Fig. 4.18: Photographs of the cyclotron feedback cooling devices. It consists of a frequency down mixer, a power splitter, and a phase shifter. The voltage controlled attenuator is not included in this figure.

Chapter 5

Experimental results

§ 5.1 Experimental setup

For the characterization of the cryogenic detection systems, a cryotest-rig is used. It consists of a two stage 4 K pulse tube cooler, which is mounted in a vacuum chamber. Photographs of the cryotest-rig and its schematic are shown in Fig. 5.1 and Fig. 5.2.

An amplifier, a resonator, and a dummy trap are mounted on the heat exchanger of the 4 K stage. This stage is surrounded by a cylindrical thermal shield, which is thermally anchored to the 40 K stage. This reduces the heat load on the 4 K stage by a factor of $(300/40)^4$ (Stefan-Boltzmann law). With this setup, it is possible to reproduce the cryogenic environment of the actual experiment. First, the characterization of the superconducting resonator is discussed.

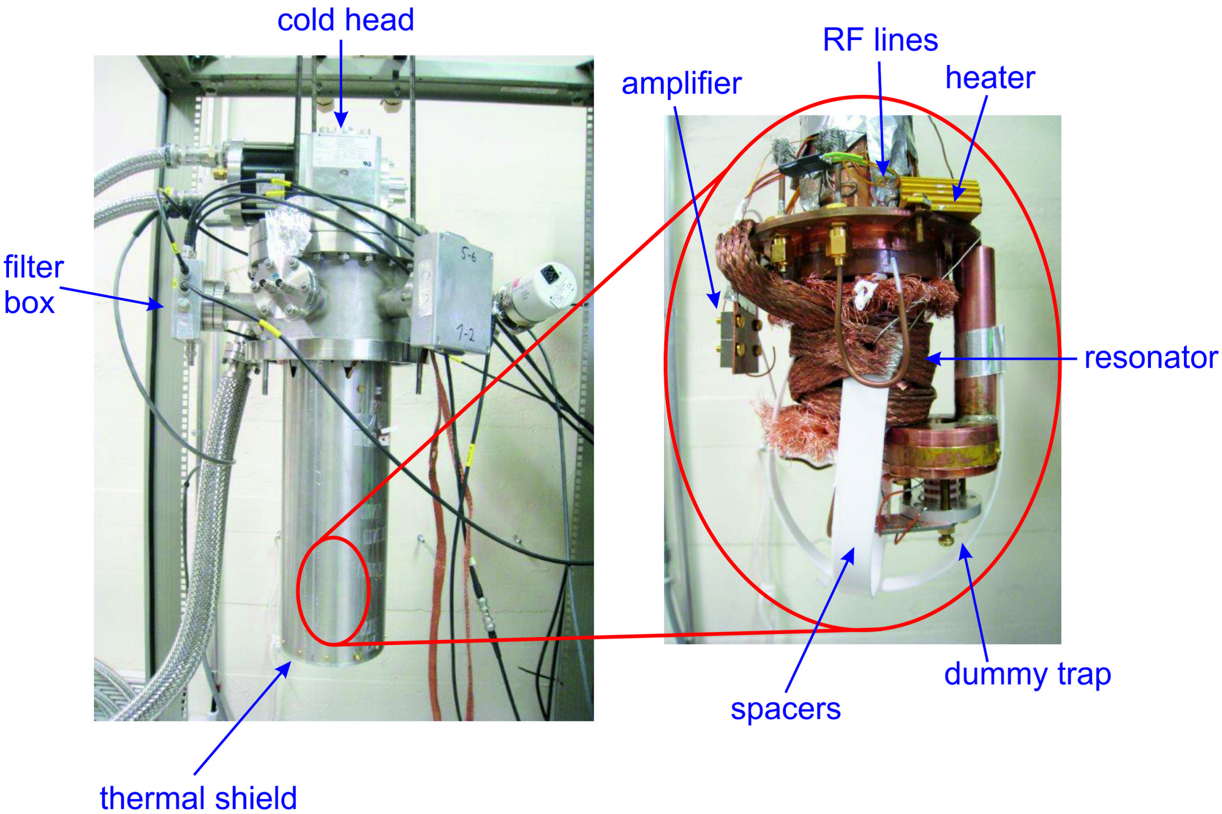

Fig. 5.1: Photographs of the cryotest-rig and the electronic devices mounted on the 4 K stage. The devices are all mounted to the 4 K stage as shown in the right photograph. In additon, heaters and temperature monitor devices are mounted in order to control the temperature. These are all wrapped around by superisolation foil before enclosed with a thermal shield. Spacers are used for preventing from those devices to touch physically to the foil, which might reduces the Q value of the detection system, due to capacitive coupling.

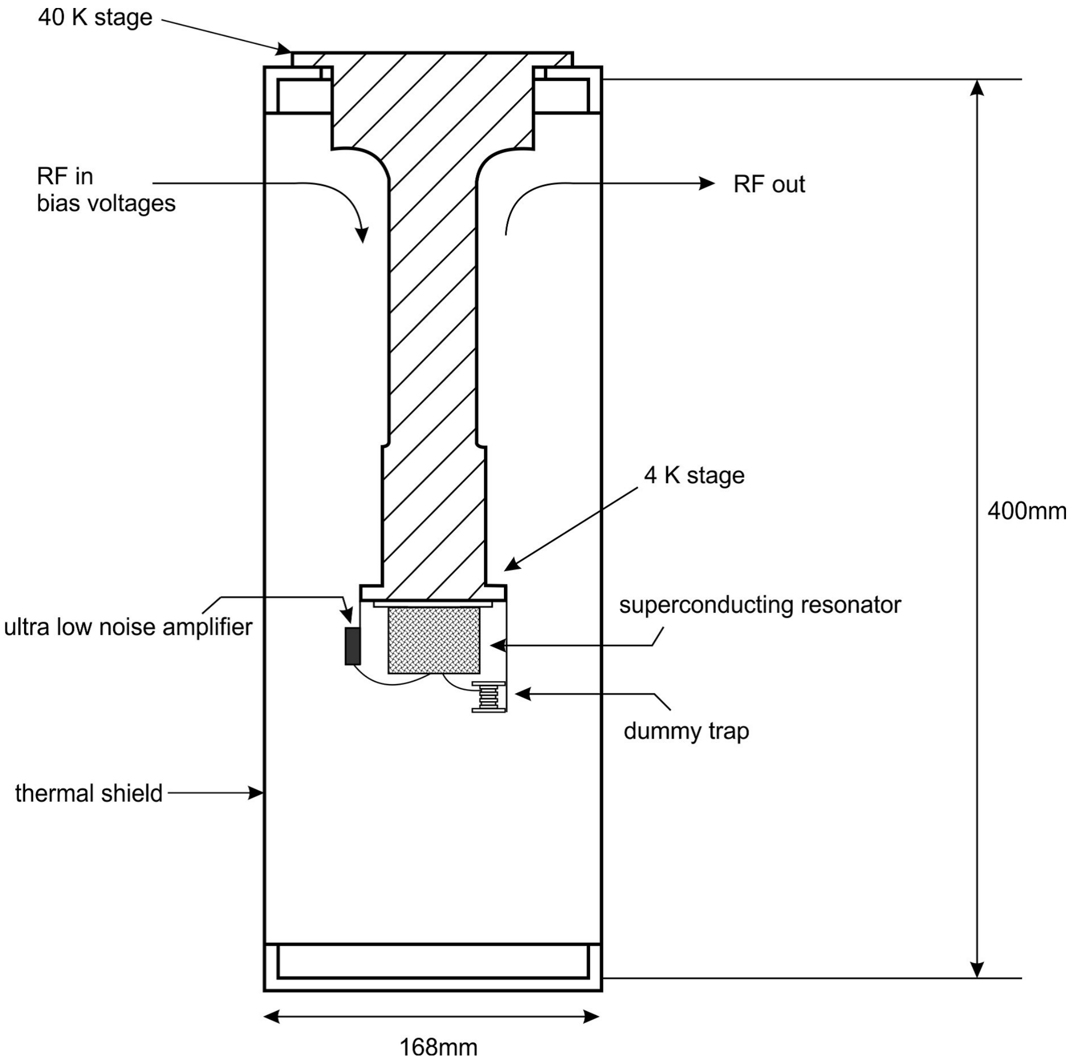

Fig. 5.2: Schematic of the cryotest-rig. It consists of a two stage 4 K pulse tube cooler. In practice, it is mounted in a vacuum chamber. RF input, RF output, and bias voltages cables are connected from the outside of the chamber to each devices.

§ 5.2 Characterization of the superconducting resonator

The superconducting toroid is mounted inside the NbTi housing as shown in Fig. 4.9. Copper braids are wrapped around the setup, which ensures proper thermalization of the superconducting housing (Fig. 5.3). It is of great importance that the superconducting surfaces are not exposed to 40 K radiation. One end of the coil is soldered to ground, while the "hot end" is thermally anchored via a sapphire feed-through. Both ensured proper thermalization of the superconducting wire. Once the cooler is switched on, it takes around 8 to 12 hours until the superconducting phase is reached.

Fig. 5.3: Photograph of the superconducting resonator being wrapped around by copper braids.

The Q-value, the inductance L, the parallel capacitance C_p, and the parallel resitance R_p of the resonator are measured with a network analyzer as shown in Fig. 5.4.

RF signals are generated from the output of the analyzer and the transmission function of the device under test is recorded. As described in section 4.1, the resonator acts as a parallel tuned circuit. Therefore, the spectrum shows a peak at the resonance frequency of the device. From the spectrum, the resonance frequency ω_0 and the Q-value can be extracted. The resonance frequency is measured by reading the peak frequency. The Q-value is obtained as follows; since the definition of the Q-value (equation (4.1)) is identical to $Q = \nu_0/\Delta\nu$, it can be extracted directly from the measured spectrum ($\Delta\nu$ is the 3 dB width of the tuned circuit's transmission function). By this measurement, one equation

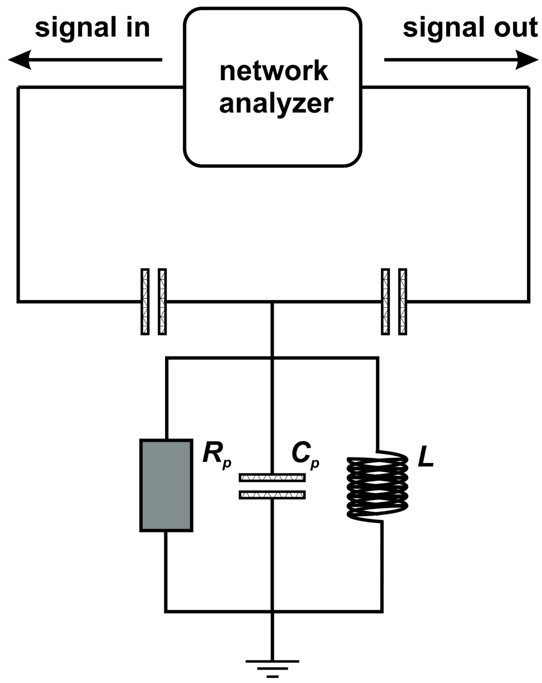

Fig. 5.4: Characterization of a resonator by using a network analyzer. A resonator is connected to the input and the output of a network analyzer. The transimission function of the resonator is recorded from this measurement.

including two variables (L and C_p) is obtained:

$$\omega_0 = \frac{1}{\sqrt{LC_p}}. \tag{5.1}$$

However, to extract L and C_p, an additional measurement is necessary, which is similar to the measurement above except for the fact that an additional capacitor is connected in parallel to the resonator. Since the capacitance of the additional capacitor C_N is known before the measurement, another equation with two identical variables is obtained.

$$\omega_1 = \frac{1}{\sqrt{L(C_p + C_N)}} \tag{5.2}$$

Likewise, ω_1 is obtained by the observed frequency spectrum, thus there are two equations with two variables. From these equations, the inductance L=1.38 mH and parallel capacitance C_p=16 pF are obtained. As described in section 4.3.1, the coil is made of a three-layer chamber winding, and has in total $N \approx 800$ turns. The inductance of a toroidal coil L is given by:

$$L = \frac{\mu_0 h(R-r)}{2\pi a} N^2, \tag{5.3}$$

with the height h of the toroid, R and r the outer and the inner radii of the toroid, and a the toroid radius to central line, respectively. With the geometrical parameters of the used toroidal coil we obtain a theoretical inductance of $L_{theory} = 1.383$ mH. This is in perfect agreement with the experimental result. To calculate the capacitance of the coil, the turn-to-turn, as well as the turn-to-shield capacitance has to be considered. Following the explanations given in [41], we obtain a theoretical coil capacitance of 15.5 pF, which is as well in very good agreement with the experimental result.

The transmission curve of the unloaded resonator, recorded with the network analyzer, is shown in Fig. 5.5. The resonance frequency is $\nu_0 = 1.069672$ MHz.

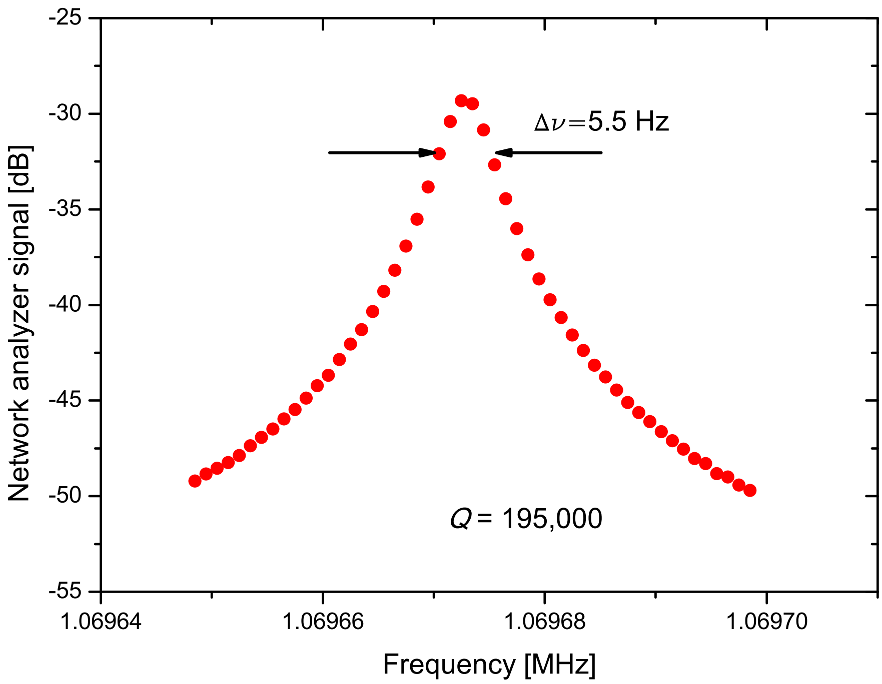

Fig. 5.5: Frequency spectrum of the superconducting resonator taken by a network analyzer with the measurement method as shown in Fig. 5.4. From this spectrum, the resonance frequency ω_0 and the Q value can be extracted directly. Doing the same scheme with an additional capacitor connected in parallel to the resonator, the inductance L and parallel capacitance C_p are obtained. For the details, refer to the text.

From this curve a quality factor of $Q = 195,000$ is extracted. This corresponds to a residual effective series resistance of only about 50 mΩ. In a 4 wire measurement of the effective series resistance with an ohmmeter with a resolution of $\mu\Omega$ no resistance could be detected. This suggests that the measured residual resistance is due to dielectric losses in the PTFE core and in the PTFE insulation of the superconducting wire. It is noted that once the resonator will be coupled to the amplifier, the Q-value of the entire system will be determined by the input characteristics of the amplifier, thus further optimization of the Q-value is not of interest. We note as well, that according to our knowledge such high Q-values have never been achieved with comparable systems. In [42] Q-values in the order 50,000 were achieved. At the BASE companion experiment at Mainz the best quality factors which were reported so far are about 40,000 for a solenoidal geometry [28] and 148,000 with a toroidal geometry [43]. At the Pentatrap experiment at the Max Planck Institute for Nuclear Physics toroidal coils with Q-values in the order of 70,000 were achieved. The measured quantities are summarized in Table 5.1.

L	C_p	ν_0	Q-value	R_p
1.38 mH	16 pF	1.069672 MHz	$\sim$195,000	1.81 GΩ

Table 5.1: Data of the unloaded superconducting resonator.

§ 5.3 Characterization of the ultra-low noise amplifiers

§ 5.3.1 Measurement method

The ultra-low noise amplifier consists of a common-source circuit for the input stage and a source-follower circuit for the output stage. Dual-gate MES-FETs are utilized for each stage. The amplifier is mounted to the pulse tube refrigerator and cooled to 4 K. Then, the gain as a function of the gate voltages and the equivalent input noise are measured. For the gain measurement, the output of a network analyzer, which generates an RF sweep is connected to the input of the amplifier, and the output of the amplifier is connected to the input of the network analyzer as shown in Fig. 5.6. The gain of the amplifier is characterized via variation of the dual-gate bias voltages of the input stage. From this method, the optimum gain (working point) is obtained.

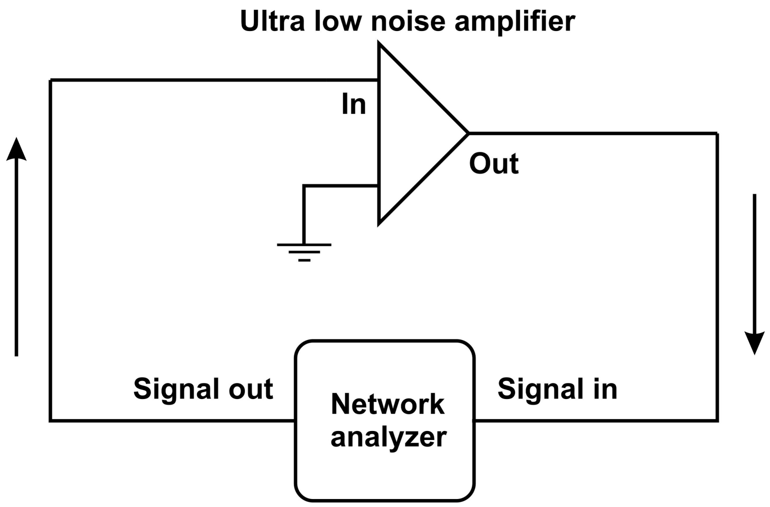

Fig. 5.6: Gain measurement of an amplifier. An amplifier is connected to the input and the output of a network analyzer. The gain as a function of the gate voltages is measured with this setup. During the measurement, other bias voltages are fixed.

For the equivalent input noise measurement, a 50 Ω termination is connected to the input of the amplifier, and a coaxial ZFL500LN amplifier is connected between the output of the amplifier and the input of a spectrum analyzer (Fig. 5.7). The 50 Ω termination is connected to prevent interference signals to couple to the input.

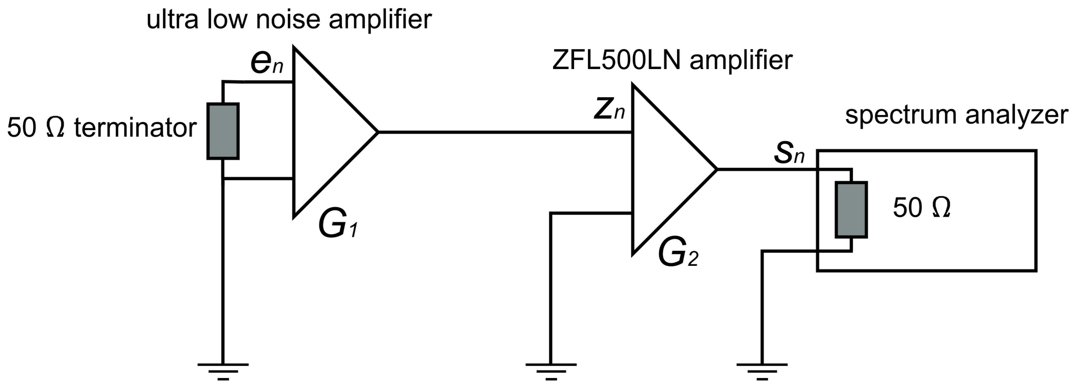

Fig. 5.7: Equivalent input noise measurement of an amplifier. A 50 Ω terminator is connected to the input of an amplifier, and a coaxial ZFL500LN amplifier is connected between the output of an amplifier and the input of a spectrum analyzer. The equivalent input noise e_n is measured by varying the gate voltages and others remain fixed. z_n is the input noise of the ZFL500LN amplifier, s_n the input noise of the spectrum analyzer, G_1 the gain of the amplifier, and G_2 the gain of the ZFL500LN amplifier, respectively.

To extract the equivalent input noise e_n from this method, it is necessary to consider the formula of the output signal u_n [V/$\sqrt{\text{Hz}}$] which will eventually be measured by using the calibrated noise marker function of the spectrum analyzer. Together with Fig. 5.7, the equation for u_n can be written as:

$$(e_n^2 G_1^2 + z_n^2) G_2^2 + s_n^2 = u_n^2. \tag{5.4}$$

G_1 is the gain of the ultra-low noise amplifier, G_2 the gain of the ZFL500LN amplifier, z_n the equivalent input noise of the ZFL500LN amplifier, and s_n the baseline noise of the spectrum analyzer, respectively. By dividing this equation by the input impedance of the spectrum analyzer R and rearranging it, the following equation is obtained:

$$\frac{e_n^2 G_1^2 G_2^2}{R} + \frac{z_n^2 G_2^2 + s_n^2}{R} = \frac{u_n^2}{R} = p_n. \tag{5.5}$$

Where p_n is the power density and the unit is dBm/Hz. The second term of the left side of this equation is the power density when only the ZFL500LN is connected to the spectrum analyzer. This can be neglected since it is factor of 100 smaller compared to u_n. Therefore, e_n [V/$\sqrt{\text{Hz}}$] is yielded:

$$e_n = \frac{\sqrt{R p_n}}{G_1 G_2}. \tag{5.6}$$

These measurements were done with several kinds of GaAs MES-FETs; CF739 (Siemens), three kinds of NE25139 (NEC), 3SK166 (SONY), and 3SK206 (NEC).

The following parameters are important to qualify the FET for our experiment: It should have a large input resistance R_{amp}, a small input capacitance C_{amp}, low power consumption and low equivalent input noise e_n. In addition, the device should be robust under numerous thermal cycles and insensitive to electric static discharge.

- The working point of the 3SK166 transistor has found to be unstable. In addition, it is very sensitive to the electrostatic discharge, and it can be easily destroyed. According to these properties, it is ruled out.
- The equivalent input noise e_n of the 3SK206 is >2 nV/$\sqrt{\text{Hz}}$. It is comparably large, which disqualifies this transistor type.
- e_n of two out of three NE25139 are ∼2 nV/$\sqrt{\text{Hz}}$, and only one of it has relatively low e_n of ∼0.65 nV/$\sqrt{\text{Hz}}$.

As a result, the CF739 and NE25139 transistors are chosen as good candidates for our experiment. In order to compare CF739 and NE25139, two amplifiers were developed. Both devices consist of a high impedance common-source input stage and a source-follower output stage for impedance matching. The output stage is based on a CF739 layout. For the input stages the two different transistors are used. These two amplifiers are characterized in the following sections.

§ 5.3.2 Comparison of the best two amplifiers

In Fig. 5.8, a schematic of the CF739 amplifier is shown. The design includes several important features:

1. Large capacitors are connected in parallel to the Gate 2 of the 1st stage FET. This prevents feedback and parasitic oscillation and is essential for stable amplifier operation.
2. A 100 MΩ resistor is applied to the Gate 1 of the 1st stage FET. It prevents the reduction of the effective parallel resistance of the detection system R_{eff}.
3. At the input, a single capacitor is applied. Together with the input capacitance C_{amp}, it defines the coupling constant κ_C (see section 4.2.2).

4. A relatively small resistor is applied to the drain bias. The drains are biased with small resistor to provide the necessary operation currents.

The schematic of the NE25139 amplifier is almost identical to the CF739 amplifier except that the Gate 2 of the first stage FET is grounded and only one capacitor is used for some RC filters whereas two capacitors are always used for the CF739 amplifier. In Fig. 5.9, photographs of those amplifiers are shown and the crucial components are indicated. For the material of the PCB board, RT/duroid 5880 is utilized for both amplifiers. The loss tangent of this board is extremely small (tan$\delta \sim 10^{-4}$), which prevents reduction of the Q value.

The gain and the equivalent input noise of the two amplifiers are measured with the schemes shown in Fig. 5.6 and Fig. 5.7. The results at optimum working conditions at a frequency of 1 MHz are summarized in Table 5.2.

FET	Gain [dB]	Equivalent Input Noise [nV/$\sqrt{\text{Hz}}$]
CF739	12.6	~0.9
NE25139	15.4	~0.65

Table 5.2: Gain and the equivalent input noise of the CF739 amplifier and the NE25139 amplifier when it set to the working point. It is measured at a frequency of 1 MHz.

In addition, the drain current I_D as a function of the Gate 1 voltage is measured to understand the behavior of the two FETs (Fig. 5.10). Other voltages are fixed as in Table 5.3.

FET	Gate 2	Drain	Source follower gate	Source follower drain
CF739	-0.6 V	3.0 V	0.0 V	1.9 V
NE25139	-	2.9 V	0.0 V	1.9 V

Table 5.3: Optimum working point of the CF739 amplifier and the NE25139 amplifier.

The optimum working point is obtained when the Gate 1 voltage is set to the point where the IV transmission has the largest slope, or in other words: at maximum transconductance. This behavior can be verified by comparing with Fig. 5.10(a) and (b) as well as (c) and (d).

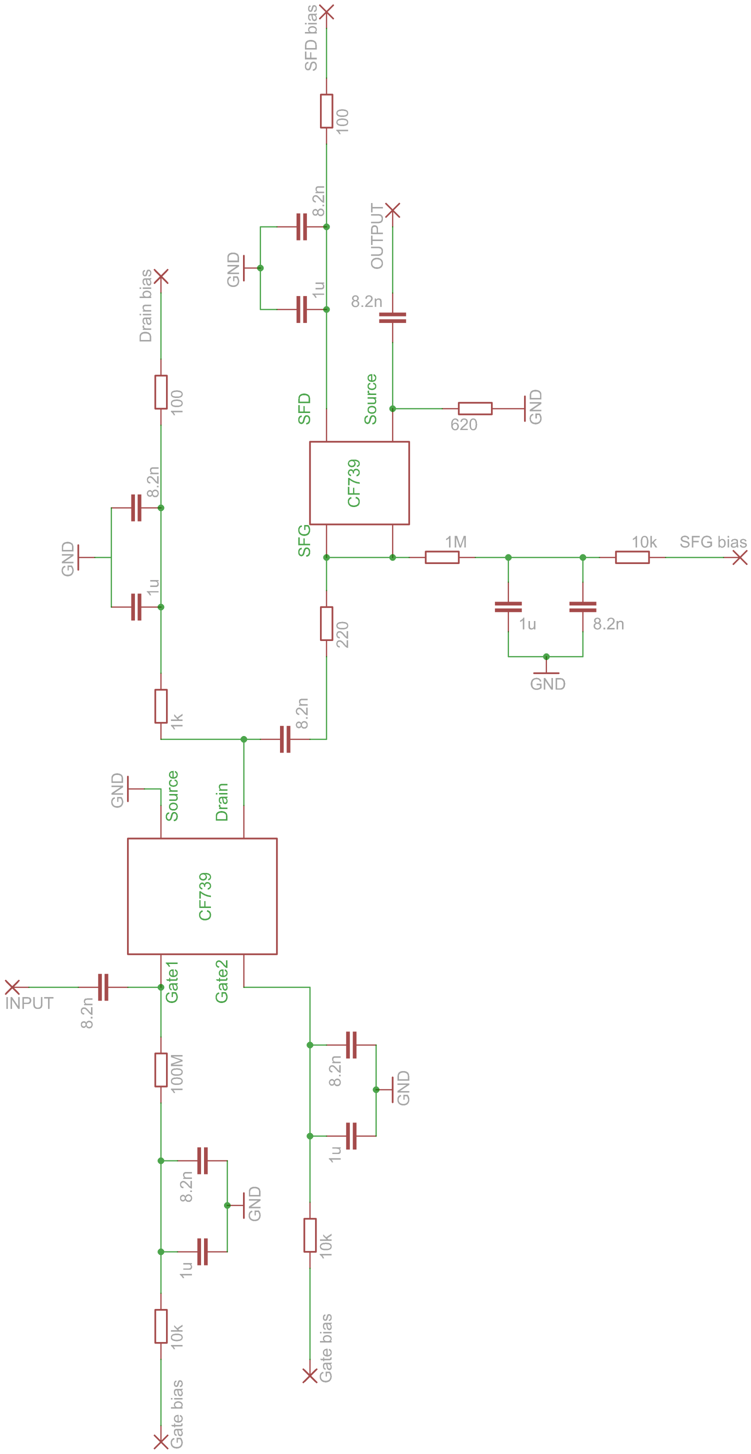

Fig. 5.8: Schematic of the CF739 amplifier. There are several tips applied as is described in the itemized text.

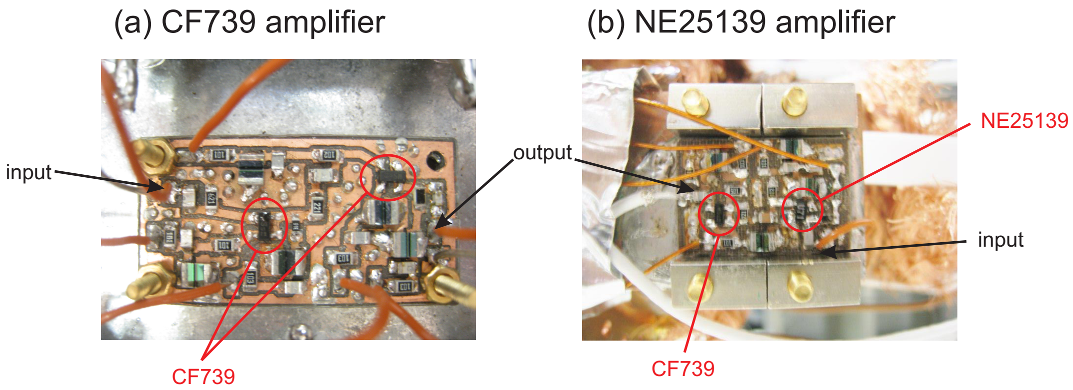

Fig. 5.9: (a) Photograph of the CF739 amplifier. (b) Photograph of the NE25139 amplifier.

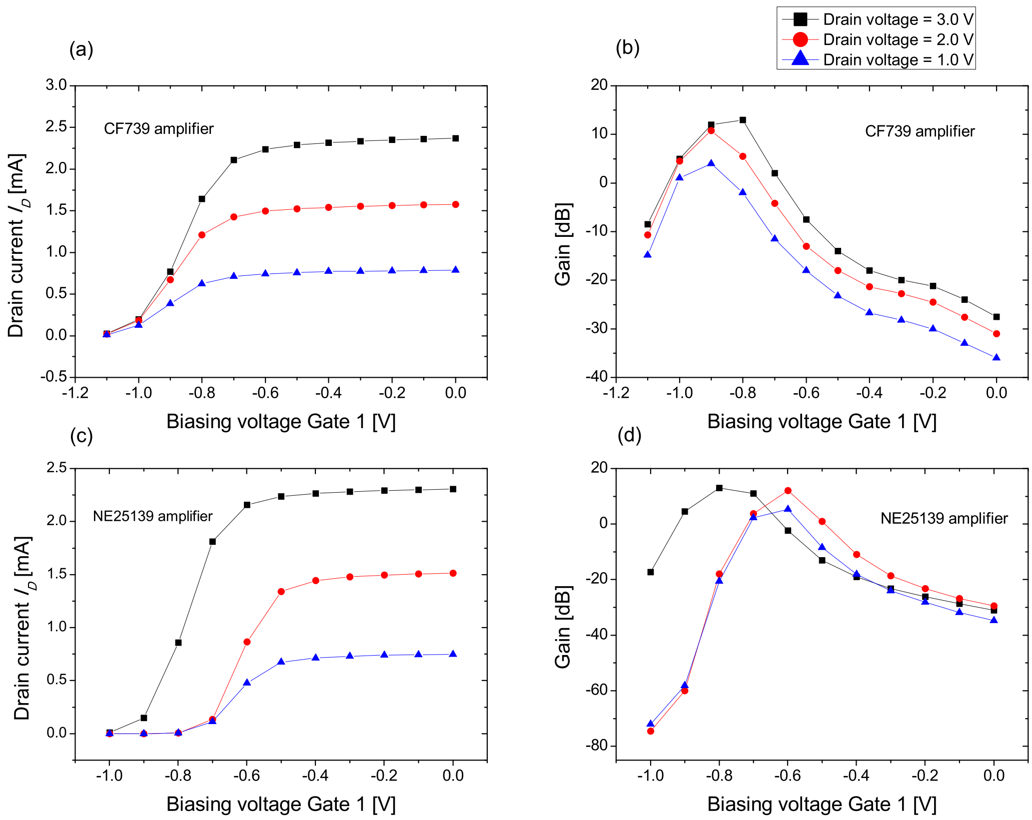

Fig. 5.10: (a) Measurement of the drain current I_D as a function of the Gate 1 voltage for the CF739 amplifier. Measured with the drain bias voltages set to 3.0 V, 2.0 V, and 1.0 V. The largest slope can be seen around -1.0 V to -0.8 V for each bias voltages. (b) Gain as a function of the Gate 1 voltage for the CF739 amplifier. Measured with the drain bias voltages set to 3.0 V, 2.0 V, and 1.0 V. There is a peak around -1.0 V to -0.8 V for each bias voltages. It can be verified that the working point can be produced at the voltage where it has the largest slope. (c), (d) Results for the NE25139 amplifier.

Next, the equivalent input noise e_n of both FETs in a range of 400 kHz to 1 MHz at the optimum working point is shown in Fig. 5.11. The noise level of the NE25139 amplifier is about a factor of 1.5 to 2.5 smaller than that of the CF739 amplifier. Moreover, the equivalent input noise of the NE25139 amplifier is almost constant in the whole frequency range. Compared to the CF739 transistor the NE25139 is better suited for the setup of sensitive single particle detection systems.

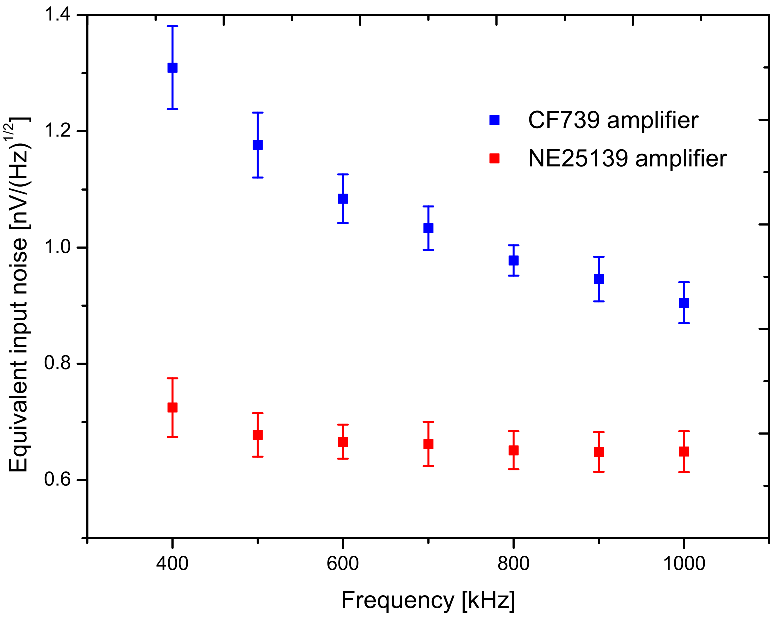

Fig. 5.11: Equivalent input noise of the CF739 amplfier (blue) and the NE25139 amplifier (red) in a range of 400 kHz to 1 MHz when it set to the optimum working point. The noise of the NE25139 amplifier is much smaller and constant over the entire frequency range.

§ 5.3.3 Amplifier noise as a function of temperature

In a next step, the behavior of amplifier noise as a function of temperature was investigated. To this end, the amplifier was cooled down to 4 K and the equivalent input noise was measured during heat-up. The results for both amplifiers are shown in Fig. 5.12.

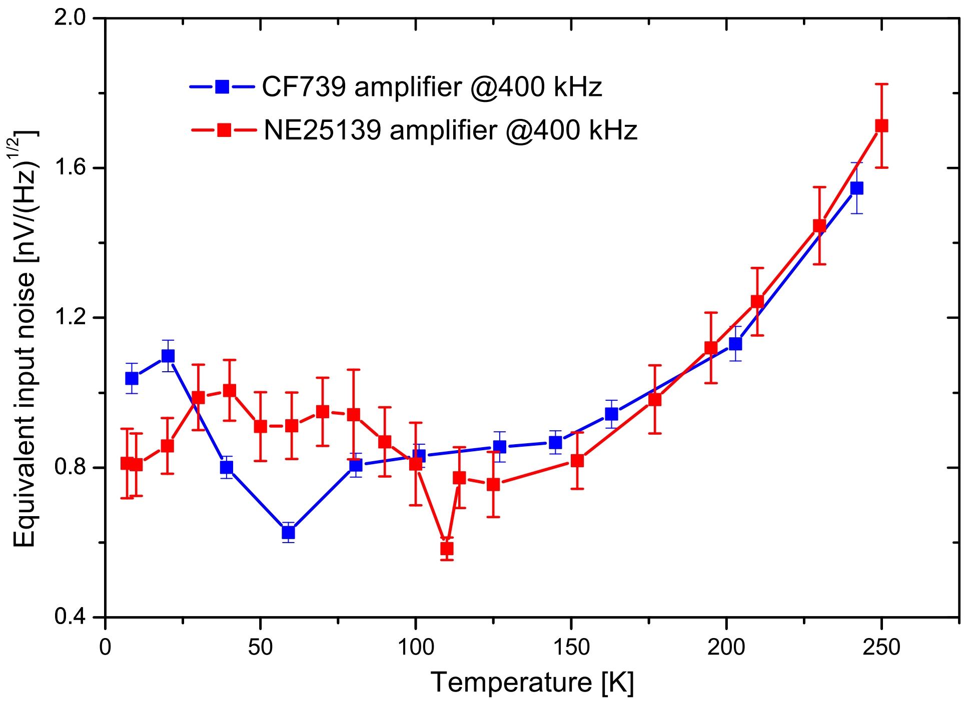

Fig. 5.12: Equivalent input noise as a fuction of the temperature for the CF739 amplifier and the NE25139 amplifier. These data is extracted from the noise of 400 kHz. For each measurements, Gate 1 voltage is varied and set to the working point.

The quality of the scaling of the two curves is almost identical. Starting from cryogenic temperatures, the noise increases up to a certain temperature, suddenly drops, and increases afterwards monotonically up to the room temperature. To understand the quality of this behavior, it is necessary to consider different sources which contribute to amplifier noise.

There are several contributions in GaAs MES-FET; the thermal noise and the 1/f noise. The thermal noise is the noise of the drain resistance, and it can be reduced by decreasing the temperature. On the other hand, 1/f noise is due to the Generation-

Recombination noise (GR noise) and the mobility fluctuations. The GR noise occurs when charge carriers are trapped in substrate impurities and released by thermal fluctuations. The GR noise is mainly present at 300 K where the thermal energy is still large enough to reactivate a trapped carrier. This noise is reduced significantly towards 4 K, where the thermal energy is often too low to release trapped carriers from the trap. The mobility fluctuations are mainly produced by defect scattering of charge carriers. Not like to the GR noise, it is not influenced very much by the temperature, and is present even at cryogenic conditions.

Thus, it can be concluded that the decrease of the noise when the temperature towards 4 K is mainly due to the reduction of the thermal noise and the GR noise. The anomalous behavior at temperatures below 100 K is not yet understood, requires further investigation, and a detailed consideration of the solid state physics of semiconductors. The available number of charge carriers in relation to different scattering effects together with scaling of transconductance with temperature has to be considered, which is beyond the scope of this thesis.

§ 5.3.4 Input characteristics of the amplifiers

For the next step, the input capacitance C_{amp} and the input resistance R_{amp} at 1 MHz are measured. C_{amp} is measured in the same way as for the measurement of the parallel capacitance of the inductor C_p (see section 5.2). R_{amp} is obtained as follows; connecting the amplifier to the inductor and measure the Q-value at known unloaded parallel resistance R_p and inductance L. Recalling the formula of the Q-value and the effective parallel resistance of the whole detection system R_{eff}, the following equations are obtained.

$$Q = \frac{R_{eff}}{\omega_0 L} \tag{5.7}$$

$$R_{eff} = \frac{R_p R_{amp}/\kappa^2}{R_p + R_{amp}/\kappa^2}. \tag{5.8}$$

From these equations, R_{amp} is calculated. See section 4.2.2 for the detail of the coupling constant κ. Resulting data of C_{amp} and R_{amp} is shown in Table 5.4.

The input capacitance C_{amp} of the two amplifiers are quite similar. However, the input resistance R_{amp} is significantly different. As discussed in section 4.2.2, R_{amp} should be as large as possible. The large R_{amp} leads to the effective parallel resistance of the

FET	Input capacitance C_{amp}	Input resistance R_{amp}
CF739	1.88 pF	3.0 MΩ
NE25139	1.95 pF	6.8 MΩ

Table 5.4: The input capacitance C_{amp} and the input resistance R_{amp} at 1 MHz for the CF739 amplifier and the NE25139 amplifier

whole detection system R_{eff} large as well. This makes the SNR large and it increases the sensitivity of the detector.

Therefore, from the fact that the NE25139 amplifier has a lower noise and higher R_{amp} compared to the CF739 amplifier, the NE25139 FET is applied for the common-source input stages of the FET circuits.

Compared to other single particle Penning trap experiments, our low noise amplifier which was developed here has a comparably high quality. this is mainly due to careful testing of different FET candidates. The NE25139 transistor which was found within this work has very low equivalent input noise at high effective input resistance and meets the requirements to construct a single particle detection system with very high quality.The amplifiers used at the BASE companion experiment at Mainz have lower input impedance but a factor of 2 larger noise. Thus the amplifier developed within this thesis has the potential to improve the sensitivity of the single particle detection systems significantly. The performance of the entire detection system and the effective improvement compared to previously developed detection systems is discussed in the next chapter.

§ 5.4 Characterization of the detection system

In a last step the performance of the entire detection system was investigated. To this end, the developed ultra-low noise amplifier was connected to the superconducting resonator and the Signal-to-Noise Ratio (SNR), as well as the Q-value was recorded as a function of amplifier biasing voltages.

§ 5.4.1 Performance of the detection system

Fig. 5.13. shows the experimental setup used to perform the measurements described in this section. The NE25139 amplifier and the superconducting resonator were connected. To adjust the coupling constant κ_c (refer to section 4.2.2) of the amplifier to the resonator, an input capacitance of 4.7 pF is used. The output of the amplifier is connected to the spectrum analyzer and the frequency spectra are recorded. The SNR is recorded for

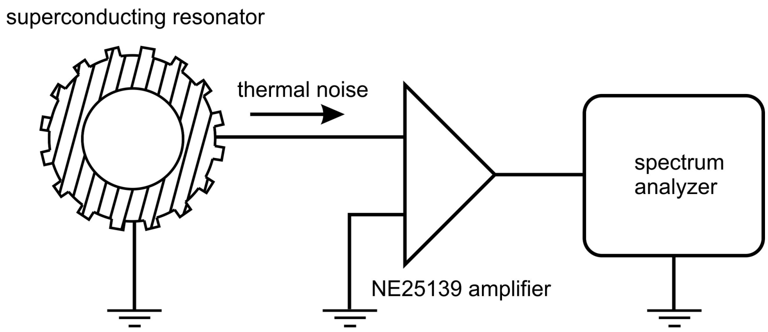

Fig. 5.13: Schematic of the SNR and the Q value measurement for the detection system. The measurement is proceeded by a spectrum analyzer instead of a network analyzer.

different Gate 1 bias voltages, whereas the other biasing voltages are fixed as in Table 5.3. The results of this measuring sequence are shown in Fig. 5.14. Noise resonances with different SNR and different Q-values are observed. At optimum biasing conditions $V_{G1} = -0.7\,\mathrm{V}$ the resulting SNR is about 32 dB at a Q-value of about 11,000. For a single particle in the catching trap this would correspond to a width of the axial frequency of about 1 Hz and would enable a measurement of the axial frequency with a resolution of 50 mHz in a measuring time of only about 10 seconds. The SNR as well as the Q-value scales with the biasing conditions of the amplifier. The observed scaling is discussed in the next section.

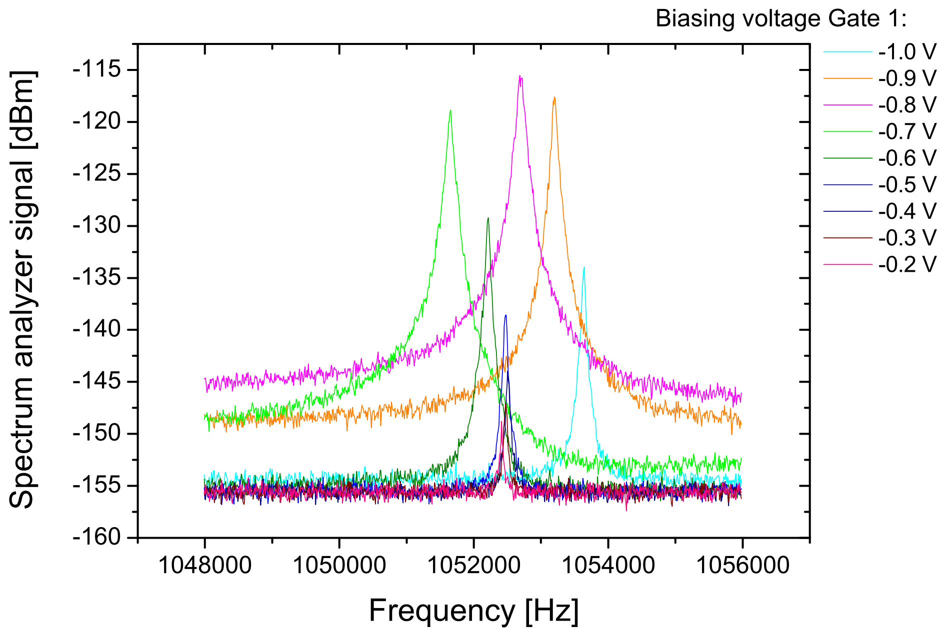

Fig. 5.14: Resonance curve of the detector. Measured for each Gate 1 bias voltages

Discussion of the SNR

The result of the SNR as a function of the Gate 1 biasing voltage is shown in Fig. 5.15.

The blue data points represent the measured results, while the red data points represent the theoretical values, which have been calculated as follows. The "signal" S [W] is due to the thermal noise of the effective parallel resistance of the detector R_{eff} and the base noise of the spectrum analyzer e_{SA}. Thus, S can be expressed as:

$$S = \frac{1}{R}(4k_B T R_{eff} \Delta B \times \kappa^2 \times G_{amp}^2 + e_{SA}^2), \tag{5.9}$$

where R is the input impedance of the analyzer, k_B the Boltzmann constant, T the temperature of the detector, ΔB the bandwidth of the analyzer input filter, κ the effective coupling constant, and G_{amp} the gain of the amplifier, respectively. On the other hand, the "noise" N [W] is due to the equivalent input noise of the amplifier e_n and e_{SA}, thus it can be written as:

$$N = \frac{\Delta B}{R}(e_n^2 \times G_{amp} + e_{SA}^2). \tag{5.10}$$

Since the NE25139 amplifier is made out of a combination of two FET circuits (common-source input stage and source-follower output stage), e_n is a function of the gain of the

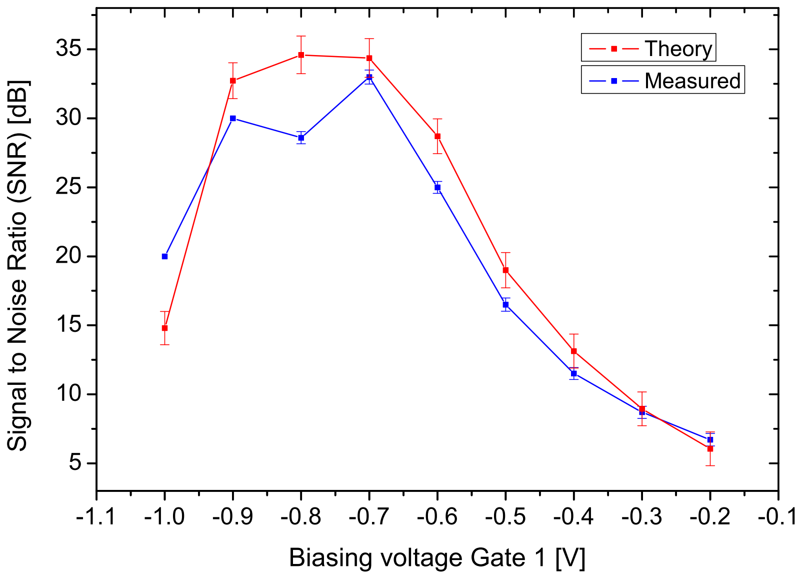

Fig. 5.15: Experimental and theoretical results of the SNR as a function of the Gate 1 bias voltages. The black line shows the measured value, whereas the red line shows the theoretical value calculated by equation.

input stage G_1 and the gain of the output stage G_2 of the amplifier:

$$e_n = \sqrt{e_{n,1}^2 + \frac{e_{n,2}^2}{G_1^2}}, \tag{5.11}$$

where $e_{n,1}$ is the equivalent input noise of the input stage, and $e_{n,2}$ the equivalent input noise of the output stage, respectively. As mentioned previously, the source-follower output stage has gain 1. Therefore, the effective gain of the amplifier can be considered as identical to the gain of the input stage:

$$e_n = \sqrt{e_{n,1}^2 + \frac{e_{n,2}^2}{G_{amp}^2}}. \tag{5.12}$$

From equation (5.12), the equivalent input noise of the amplifier e_n has the smallest value when G_{amp} is maximized. In Fig. 5.16, it shows e_n as a function of the Gate 1 bias voltage for the NE25139 amplifier. This behavior can be seen together with Fig. 5.10(d).

When G_{amp} is large enough so that the baseline noise of the analyzer e_{SA} can be neglected, the SNR can be written as:

$$SNR = \frac{S}{N} = \frac{\sqrt{4k_B T R_{eff}}}{e_n} \times \kappa_l \kappa_c = \sqrt{\frac{4k_B T R_{eff}}{e_{n,1}^2 + e_{n,2}^2/G_{amp}^2}} \times \kappa_l \kappa_c. \tag{5.13}$$

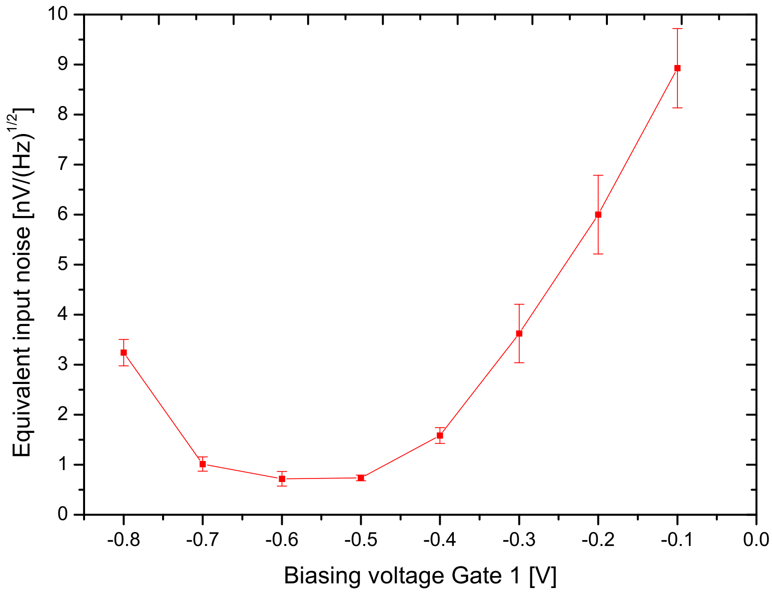

Fig. 5.16: Equivalent input noise as a function of the Gate 1 voltage for the NE25139 amplifier.

As described by equation (5.13), the smaller the equivalent input noise of the amplifier e_n is, the larger the SNR will be. This can be verified by Fig. 5.15 and Fig. 5.16. By inserting the measured values of the resonator and the amplifier (table 5.5, table 5.6) to equation (5.13), and together with Fig. 5.10(d), the red data points in Fig. 5.16 are obtained.

	R_p	κ_l
Superconducting resonator	1.7 GΩ	0.25

Table 5.5: Observed quantities of the superconducting resonator. Where R_p is the parallel resistance and κ_l the coupling constant (refer to section 4.1).

At low amplifications, the background noise of the spectrum analyzer contributes as well as the noise produced by the source-follower output stage, and thus can not be neglected, leading to a decrease in SNR. Once the gain of the amplifier increases, and $e_n G_{amp}$ exceeds the spectrum analyzer noise level, the SNR increases as well. The theoretical values reproduce the the scaling of the measured values perfectly, however, a slight offset between the measured values and the theoretical values is observed. In

	R_{amp}	e_n	κ_c
NE25139 amplifier	6.8 MΩ	0.65 nV/$\sqrt{\text{Hz}}$	0.71

Table 5.6: Observed quantities of the NE25139 amplifier. R_{amp} is the input resistance, e_n the equivalent input noise, respectively (refer to section 4.1).

order to understand this effect, further evaluation of the data for the Q-value is required. Possible reasons for this slight discrepancy will be discussed in the next section.

Discussion of the Q-value

The Q-value as a function of the Gate 1 biasing voltage is shown in Fig. 5.17(a). For biasing voltages between -0.2 V and -0.5 V it is constant within error bars. Beyond -0.5 V, it decreases in the range of maximum amplification (~ -0.75 V) and increases towards even smaller voltages. In Fig. 5.17(b), the transconductance gm of the FET is shown as a function of the Gate 1 biasing voltage. At maximum g_m, when it has the largest amplification, the lowest Q-value is reached.

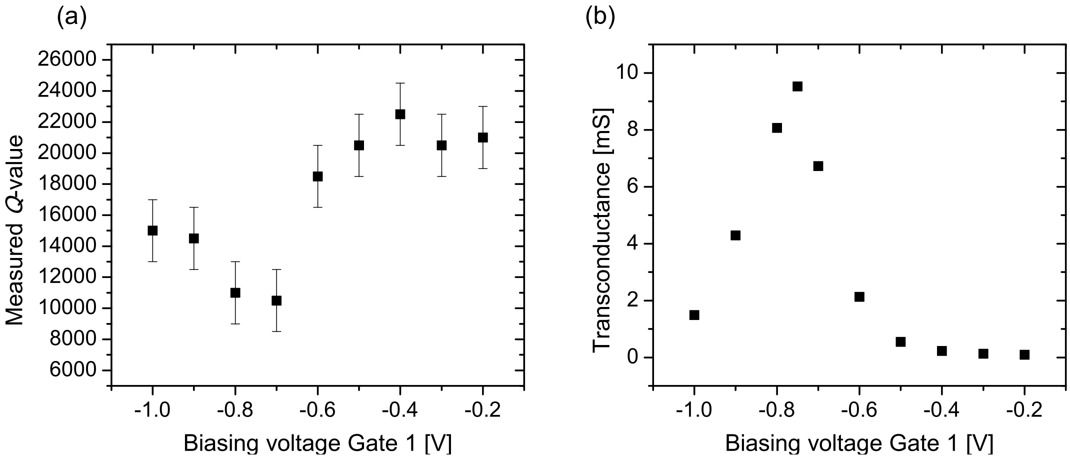

Fig. 5.17: Q-value (a) and transconductance (b) as a function of Gate 1 biasing voltage. For a detailed discussion, refer to the text.

This behavior is well understood and known as the Miller effect. The inverted amplified signal is fed back to the input via a intrinsic parasitic capacitance C_{GD} between the drain and the gate of the amplifier. Mathematically this regeneration effect can be described by considering a model FET with ideal g_m, the parasitic capacitance C_{GD}, and output load resistor R_D as shown in Fig. 5.18.

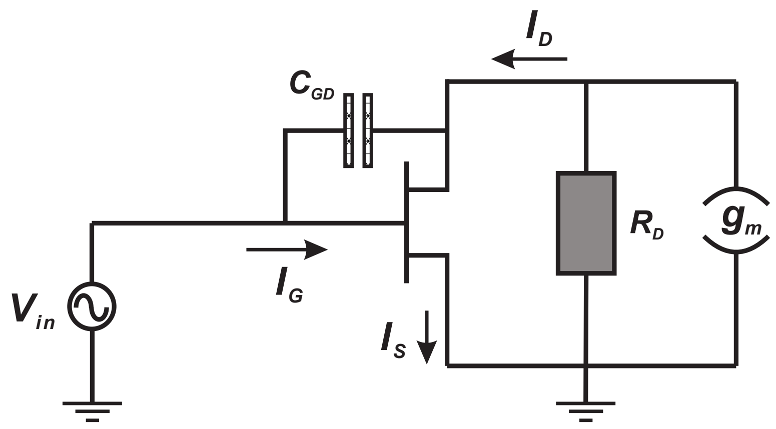

Fig. 5.18: Schematic of a FET which considered C_{GD}.

There are four equations to describe the behavior of this model.

$$I_G + I_D = I_S \tag{5.14}$$

$$I_G = \frac{V_G - V_D}{Z_{GD}} \tag{5.15}$$

$$I_S = g_m V_G \tag{5.16}$$

$$V_D = -I_D R_D \tag{5.17}$$

where Z_{GD} represents the impedance of the gate to drain capacitance. Therefore, together with equations (5.14) $\sim$ (5.17), the input impedance of this circuit $Z_{in} = V_G/I_G$ can be expressed as:

$$Z_{in} = \frac{R_D + 1/(2\pi j \nu_0 C_{GD})}{1 + g_m R_D} \tag{5.18}$$

Equation (5.18) indicates that the input impedance Z_{in} is a combination of the input series resistance R_S and the input series capacitance C_S as shown in Fig. 5.19. R_S and C_S are expressed as:

$$R_S = \frac{R_D}{1 + g_m R_D} \tag{5.19}$$

$$C_S = (1 + g_m R_D) C_{GD} \tag{5.20}$$

It can be converted into an effective parallel input by following simple algebra. In addition, Fig. 5.19 is converted to Fig. 5.20.

$$R_{amp} = \frac{1 + 4\pi^2 \nu_0^2 R_S^2 C_S^2}{4\pi^2 \nu_0^2 R_S C_S^2} \tag{5.21}$$

$$C_{amp} = \frac{C_S}{1 + 4\pi^2 \nu_0^2 R_S^2 C_S^2} \tag{5.22}$$

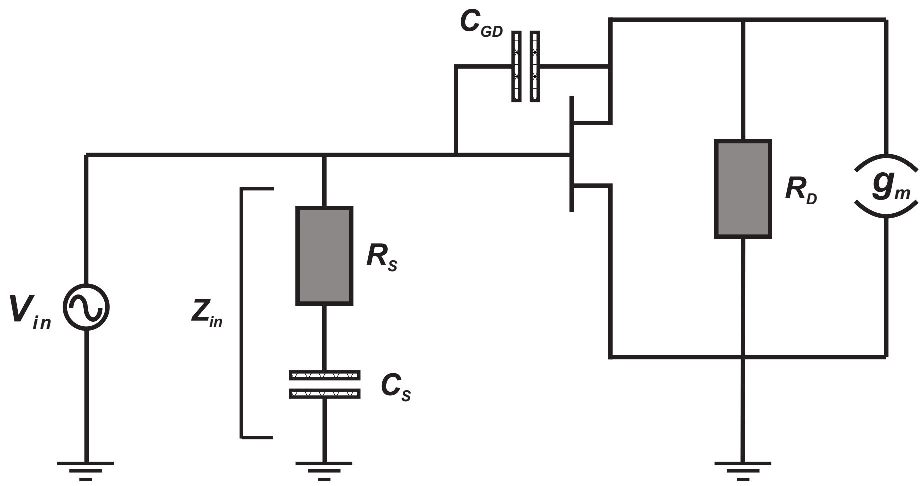

Fig. 5.19: Schematic of a FET which considered C_{GD} and the input series impedance Z_{in}.

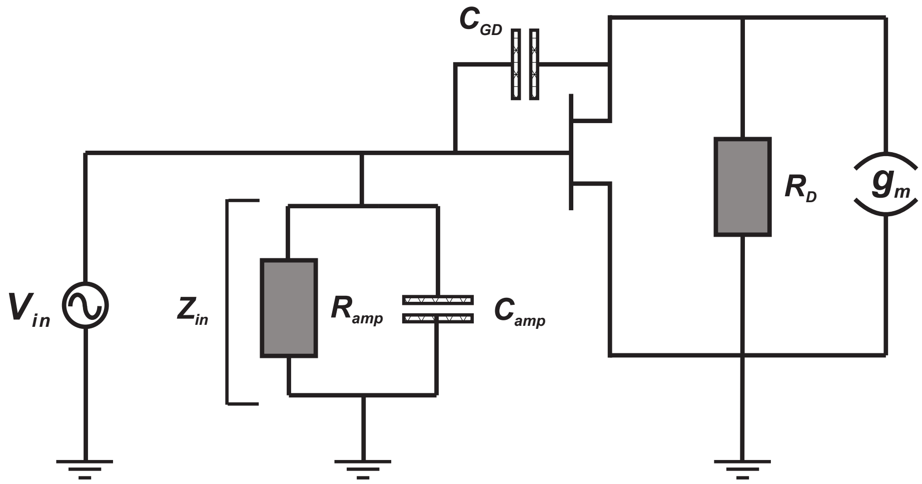

Fig. 5.20: Schematic of a FET which derived from Fig. 5.19 and equation (5.21), (5.22). This figure indicates that C_{GD} couples R_D and adds a resistive ingredient R_{amp} to the input, reducing the Q-value of the resonator.

As indicated in Fig. 5.20, C_{GD} couples the output load of the amplifier which adds a resistive ingredient R_{amp} to the input, reducing the Q-value of the resonator.

By using equations (5.19) $\sim$ (5.21), the measured transconductance, a feedback capacitance $C_{GD} = 0.65$ pF, an additional input resistance $R_{in,p} = 9.2$ MΩ which accounts for dielectric loss effects in the board material, and a load resistance $R_D = 1300\ \Omega$ (value of the 1000 Ω work resistor cooled to 4 K), we obtain the effective input resistance of the amplifier R_{amp} as shown by the red points in Fig. 5.21. In Fig. 5.22, it shows the equivalent circuit of the whole detection system which also considered the Miller effect.

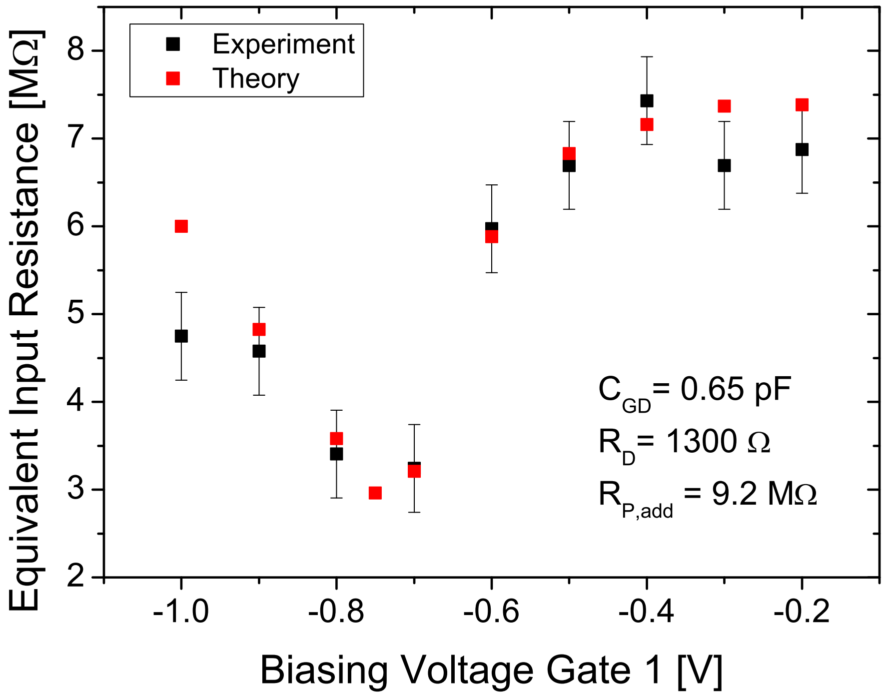

Fig. 5.21: Effective input resistance of the amplifier as a function of the Gate 1 biasing voltage. The black data points represent the measured data, the red data points are due to theoretical calculations using the simple transconductance model described in the text.

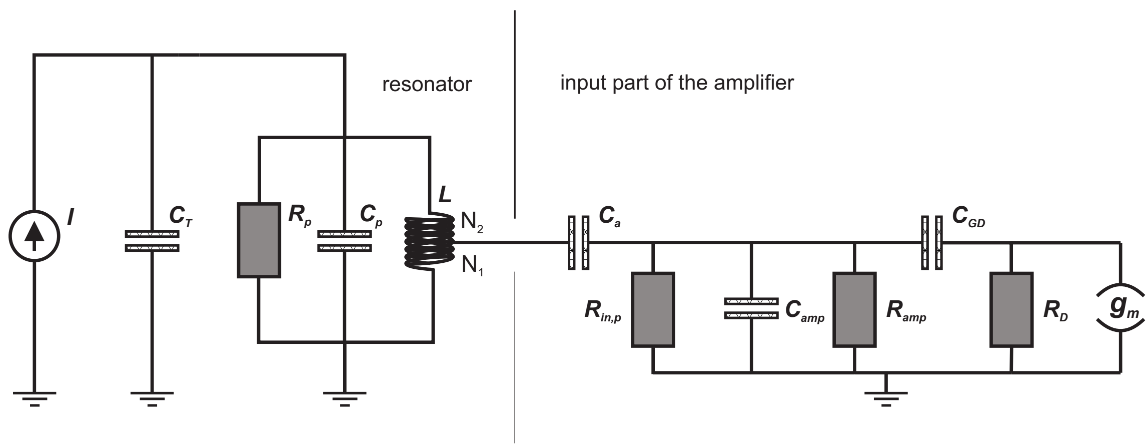

Fig. 5.22: Equivalent circuit of the whole detection system by considering the Miller effect.

The model calculation is in very good agreement with the measured results, except for very low biasing voltages. This slight discrepancy arises from the fact the at these biasing voltages the drain to source channel resistance increases dramatically, effectively changing R_D, which leads to an additional damping of the Q-value of the resonator. The described decrease of the input resistance at highest gain explains the slight discrepancy of the theoretical and the experimental SNR mentioned in the previous section very well. In conclusion, the behavior of the detection system tested here is very well understood. A slight regeneration effect is observed, however, in the optimum working point the detector provides stable operation at Q-values in the order of 11000 and SNR of 32 dB, corresponding to a significant improvement compared to previously used detectors. The observed regeneration effect could be suppressed by operating the second gate as a cascode circuit. However, at the final operation frequencies of about 750 kHz the feedback effect will be suppressed since feedback reactance will decrease. Thus, in a next step the detector will be connected to a test Penning trap to reproduce the conditions of the experimental setup.

§ 5.4.2 Detection system connected to a test Penning trap

In this step, the detection system was connected to a 5 electrode test Penning trap, which is similar to the traps used in the BASE experiment. The measurement method is shown in Fig. 5.23. Similar measurements as above were performed, however, the 14 pF capacitance of the trap shifts the effective resonance frequency to about 738 kHz.

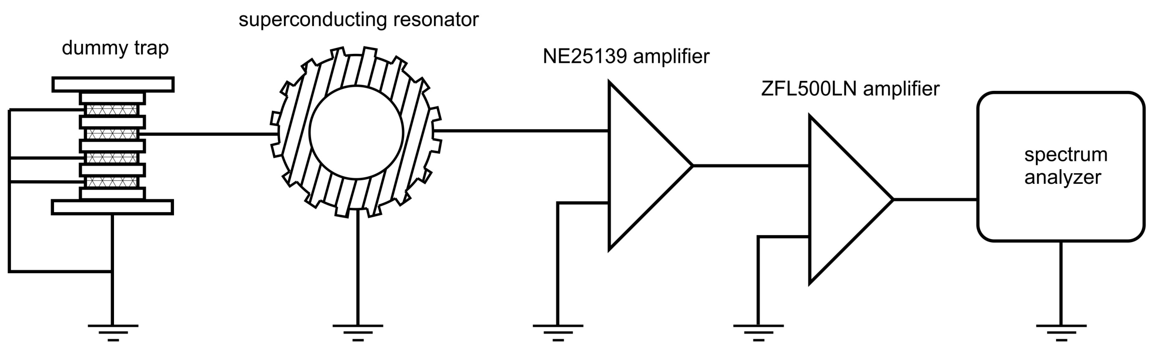

Fig. 5.23: Schematic of the SNR and the Q value measurement for the detection system connected to a test Penning trap. With this measurement, ZFL500LN amplifier is connected between the NE25139 amplifier and the spectrum analyzer.

In this lower frequency range the feedback effect is expected to be suppressed significantly. Results of the quality factor as a function of the Gate 1 biasing voltage are shown in Fig. 5.24.

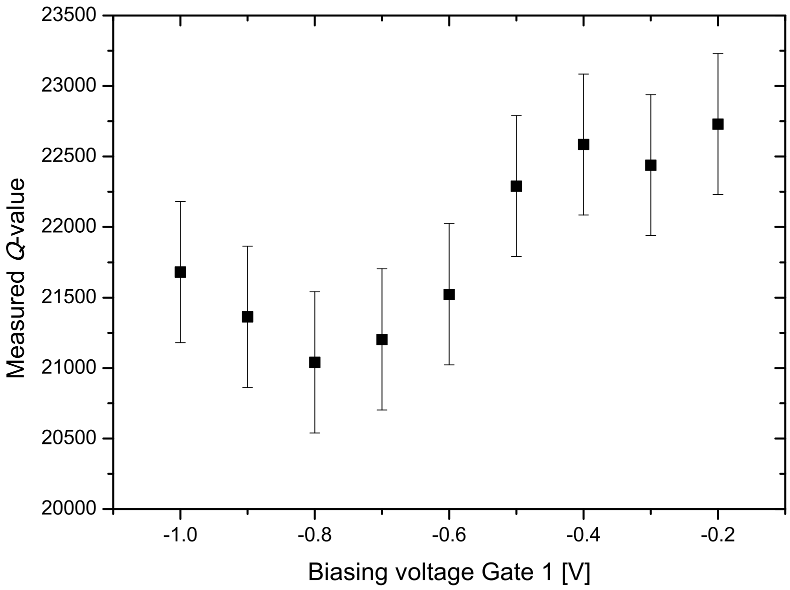

Fig. 5.24: Q-value of the detection system connected to the test Penning trap as a function of the Gate 1 biasing voltage. For a detailed discussion, refer to the text.

A higher quality factor as well as a weaker scaling of the Q-value as a function of the V_{G1} is observed. The weaker scaling of $Q(V_{G1})$ is as expected. The higher Q-value which was achieved in these measurements is due to the fact that the effective Miller reactance is suppressed by a factor 1070000/738000, and thus, the coupling of the amplifier load to the resonator. A spectrum of the detector signal with the trap connected is shown in Fig. 5.25. We have obtained SNR = 34.5 dB at a Q-value of about 21000, which corresponds to an effective parallel resistance of the entire detection system of about $R_p = 132\ \mathrm{M\Omega}$.

The detection system for the Precision trap which was developed recently at the BASE companion experiment at Mainz has a SNR of 20 dB at a Q-value of about 12,500 [comparison]. Compared to this the SNR is improved by 15dB. The relevance of this further improvement can be discussed quantitatively by comparing the expected frequency scatter obtained from the frequency scatter of the dip for similar averaging time Tavg (refer

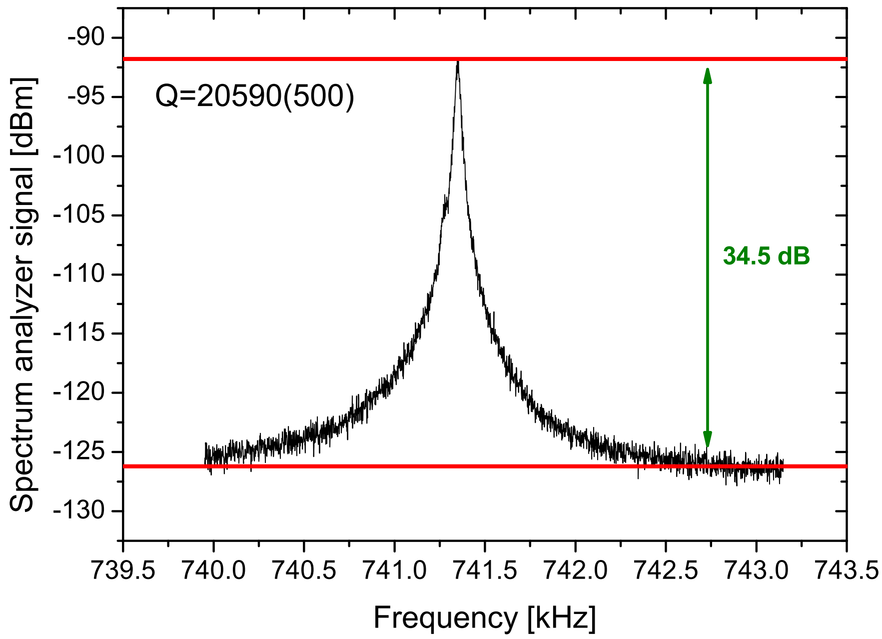

Fig. 5.25: Spectrum of the detector signal when it is connected to the test Penning trap. We obtained the SNR of 34.5 dB

to section 4.2.1). Together with equation (4.19) we obtain:

$$\frac{\sigma_{BASE}}{\sigma_{Mainz}} \approx \sqrt{\frac{\Delta\nu_{BASE}}{\Delta\nu_{Mainz}}} \times \sqrt{\frac{SNR_{Mainz}}{SNR_{BASE}}} = 0.76. \tag{5.23}$$

From above, the expected frequency scatter of the detection system we have developed in BASE is smaller than that used at Mainz. Thus, frequency measurement cycles reduce from currently about 60 s to 30 s. This indicates that the results of the BASE-CERN experiment will be less sensitive to systematic drifts. Therefore, at the moment the BASE-Mainz experiment has a limited spin flip fidelity of only about 75 %, which is caused by an axial frequency scatter caused by jumps in the cyclotron quantum state, which are on the order of 3 quantum-jumps per minute. Once the axial frequency can be measured much faster, the spin flip detection fidelity is increased and a g-factor measurement with much higher resolution becomes possible. The prototype detection system described in this thesis is among other developments and will be a basis to reach the goal of measuring the antiproton magnetic moment with high precision.

Chapter 6

Ultra high precision voltage source

A single spin transition in the Analysis trap shifts the axial oscillation frequency by only 190 mHz out of about 600 kHz. The axial frequency is defined by a voltage V_0 applied to the ring electrode of the Penning trap.

$$\omega_z = \sqrt{\frac{2qC_2V_0}{m}} \tag{6.1}$$

where q is the charge, m the mass, and $\sqrt{C_2}$ a trap specific length, respectively. Thus, the detection of single antiproton spin transition requires ultra-high stability of the voltages used for biasing of the trap electrodes. To this end, ultra-high precision voltage sources which were specifically developed for BASE (Stahl Electronics) are used (Fig. 6.1). In this chapter, the characterization of the voltage sources is described, as well as the temperature stabilization system which has been designed in the framework of this thesis.

§ 6.1 Characterization of UM 1-14

There are three primary channels ($0 \sim 14$ V range), three secondary channels for providing a smaller voltage range (diminished by a factor of 4) which are coupled to the primary channels by internal voltage dividers, and 10 add-on auxiliary channels which are intended for no need of extreme stability. The primary and secondary output channels can be run either in *ultra high precisionmode* (featuring highest resolution and stability) or in *fast mode*. The latter is internally only 16 bit resolved, features less accuracy but faster response time (for instance, suited for transporting antiproton to other traps). The former

Fig. 6.1: Photograph of the ultra-high precision voltage source UM 1-14 (Stahl Electronics). It is necessary to have a high voltage stability, since the voltage fluctuation is directly related to the axial frequency fluctuation. If the axial frequency fluctuation is too large, it makes difficult to resolve the axial frequency shift caused by a single spin transition.

offers 25 bit of higher resolution and stability.

To characterize the voltage stability, the voltage and the temperature of the UM 1-14 are measured simultaneously by the LABVIEW program for a long sequence of time. The LABVIEW program and the results are shown in Fig. 6.2 and Fig. 6.3.

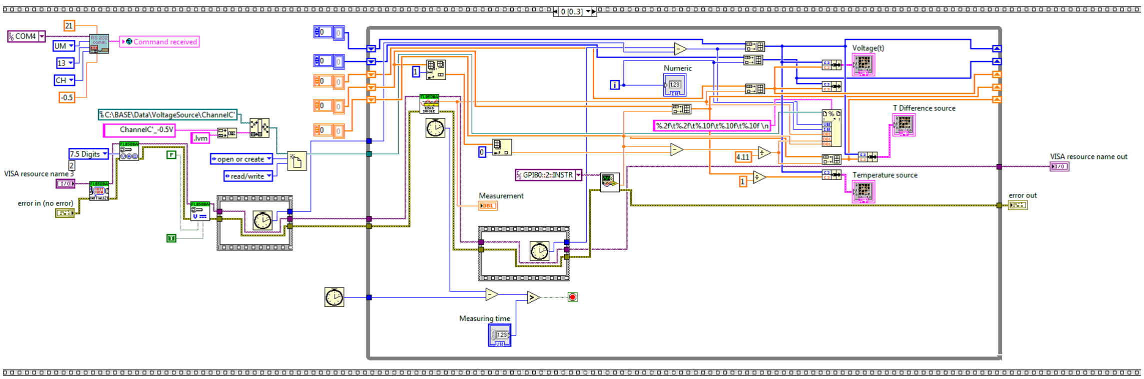

Fig. 6.2: LABVIEW program used for measuring the voltage and the temperature of the UM 1-14 simultaneously.

By comparing Fig. 6.3.(a) and Fig. 6.3(e), it is obvious that there are two different kinds of voltage fluctuations. A fluctuation due to temperature drifts, and and short term fluctuations, presumably arising from electronics noise in the utilized voltage references. The former can be easily characterized by plotting the voltage as a function of the temperature and make a fit with a linear function as it is shown in Fig. 6.3(f). From the fit

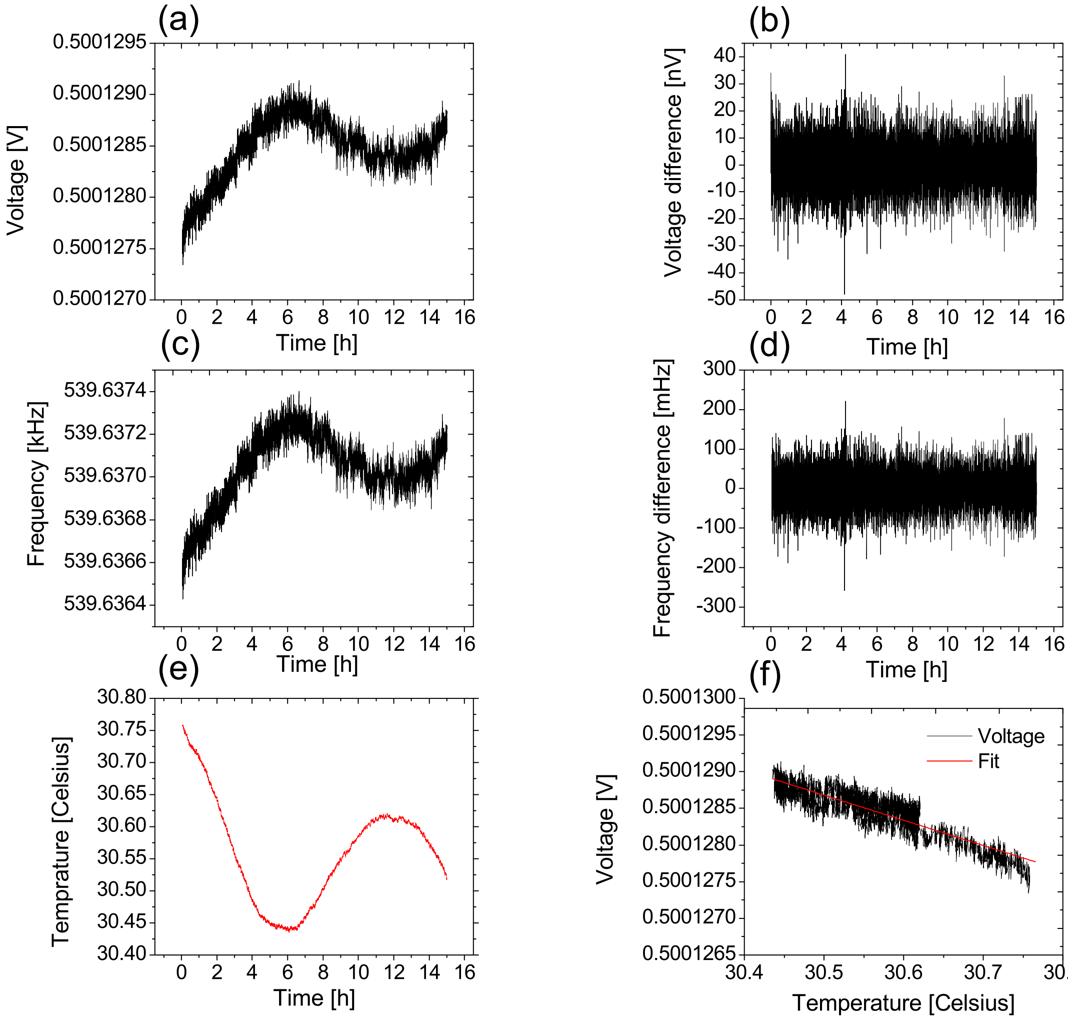

Fig. 6.3: (a) Measurement of the voltage (-0.5 V) as a function of time. Small fluctuation is due to the voltage source instability. (b) Voltage difference obtained from (a). (c) Frequency as a function of time which is calculated from equation (6.1). (d) Frequency difference obtained from (c). (e) Temperature as a function of time. (f) Voltage as a function of temperature, which obtained from using (a) and (e). By making a fit with a linear function to (f) and evaluating it, 1.8 Hz/K of axial frequency fluctuation due to the temperature fluctuation is obtained.

function, the slope of -3.4 μV/K is obtained. Together with equation (6.1), it is pointing out that the axial frequency will shift about 1.8 Hz when the temperature drifts by 1 K. Since the axial frequency shift due to the spin transition is about 190 mHz and it takes about 30 seconds to resolve it, temperature stability of 0.3 mK/sec is required. To this end, an apparatus which maintains the stability of the temperature must be constructed. This will be discussed in section 6.2.

On the other hand, the voltage fluctuation due to the UM 1-14 itself is evaluated via the Allan variance. The Allan variance is the most common time domain measure of stability. It is intended to estimate stability due to noise processes. The function of the original Allan variance can be written as:

$$\sigma^2(\tau) = \frac{1}{2(N-1)} \sum_{i=1}^{N-1} [A_{i+1} - A_i]^2 \tag{6.2}$$

Where A_i is the ith of M fractional values averaged over the measurement interval, τ. Therefore, A_i can be easily expressed as;

$$\begin{aligned} A_i &= \frac{1}{a} \sum_{k=1}^{a} \Delta V_k \ (i = 1 \sim N - a) && (6.3) \\ \Delta V &= V_{i+1} - V_i \ (i = 1 \sim N - 1) && (6.4) \\ \tau &= 6a \ (a = \text{natural number}) && (6.5) \end{aligned}$$

Where N is the number of measuring points and V_i the ith of measured voltage. τ is expressed as in equation (6.5), since the voltages are measured in every 6 seconds. The results for $a = 1, 2, 3, 4, 8, 16, 24$ are shown in Fig. 6.4.

As mentioned in the last part of chapter 5, it is expected to take about 30 seconds to measure the axial frequency by using the developed detection system. From Fig. 6.4, the frequency fluctuation due to the UM 1-14 itself is around 10 mHz in 30 seconds measuring time interval τ. Therefore, this fluctuation is negligible for our experiment. In Fig. 6.5, it shows data when -1.0 V is supplied from the UM 1-14. Likewise, it has similar fluctuations and its scaling is identical to the measurement for 0.5 V. Therefore, only the fluctuation due to the temperature shift should be taken into account.

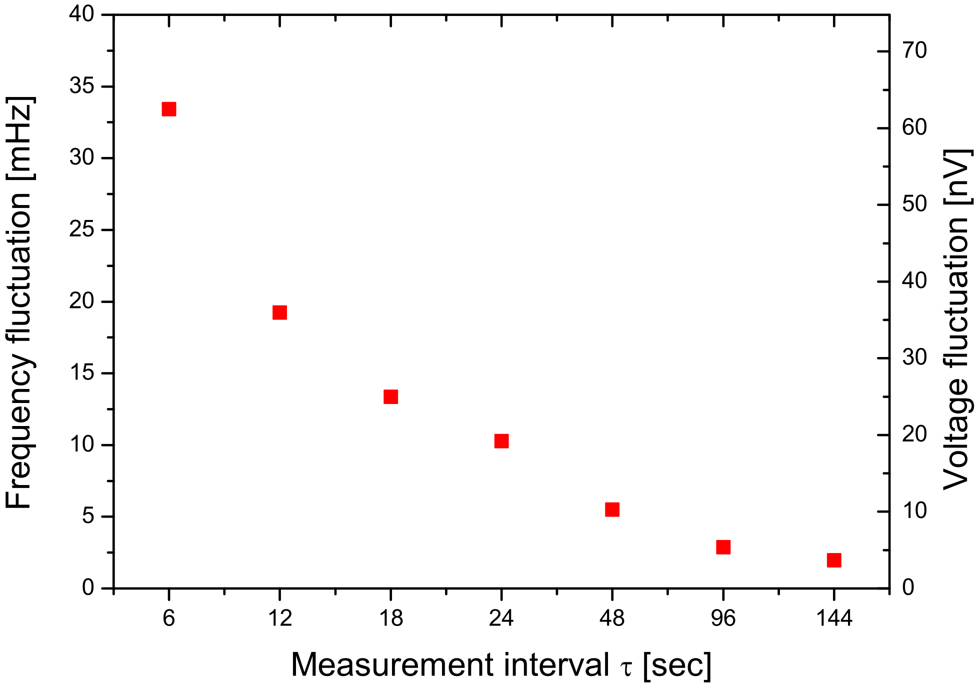

Fig. 6.4: Frequency fluctuation and voltage fluctuation of the UM 1-14 evaluated by using the original Allan variance. It has been calculated for $a = 1, 2, 3, 4, 8, 16, 24$.

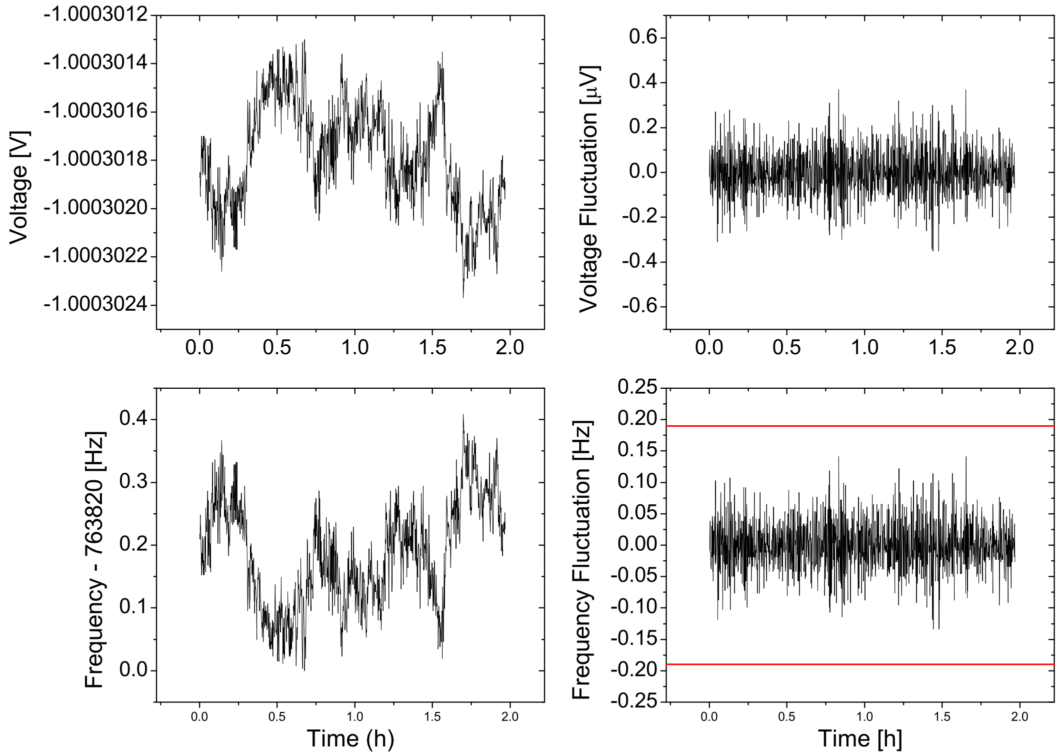

Fig. 6.5: (a) Measurement of the voltage (1.0 V) as a function of time. (b) Voltage difference obtained from (a). (c) Frequency as a function of time. (d) Frequency difference obtained from (c).

§ 6.2 Development of the temperature stabilization apparatus

To stabilize the temperature of the UM 1-14, a temperature stabilization box is constructed. Its framework is made out of aluminum ITEM profiles, and enclosed by acrylic plates. Inside of this box, three UM 1-14 will be mounted as shown in Fig. 6.5. Fig. 6.5(a) shows the schematic of the box, and Fig. 6.5(b) shows its photograph. In addition, several temperature sensors and a heater will be mounted inside of it. A temperature sensor is attached to the outside part of one of the acrylic plates. The heater is used to maintain the same temperature inside of this box. Currently, the heating system is under development.

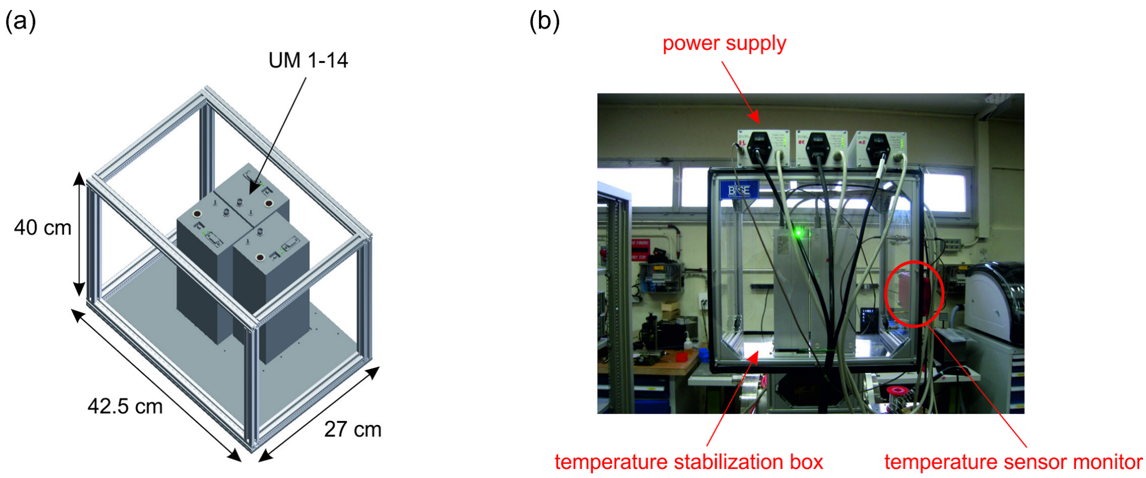

Fig. 6.6: (a) Schematic of the temperature stabilization box. Three UM 1-14 are mounted inside with temperature sensors, and enclosed by acrylic plates. (b) Photograph of the temperature stabilization box. Power supplies for each UM 1-14 will be placed on top of the box. On one of the side of the acrylic plates, temperature sensor monitor will be attached.

Under the box, an RF box is placed. Inside the RF box two filter boards are attached, which clean spurious RF noise from the UM 1-14. There are 24 channels of RC filters for each board. Those are enclosed by the RF box to prevent from external noises to intrude on to cables inside. Fig. 6.6 shows a diagram of how voltages are cleaned by the two filter-boards. The temperature stabilization apparatus is still under development. For the further step, it is necessary to develop a control system for maintaining the constant temperature inside the apparatus.

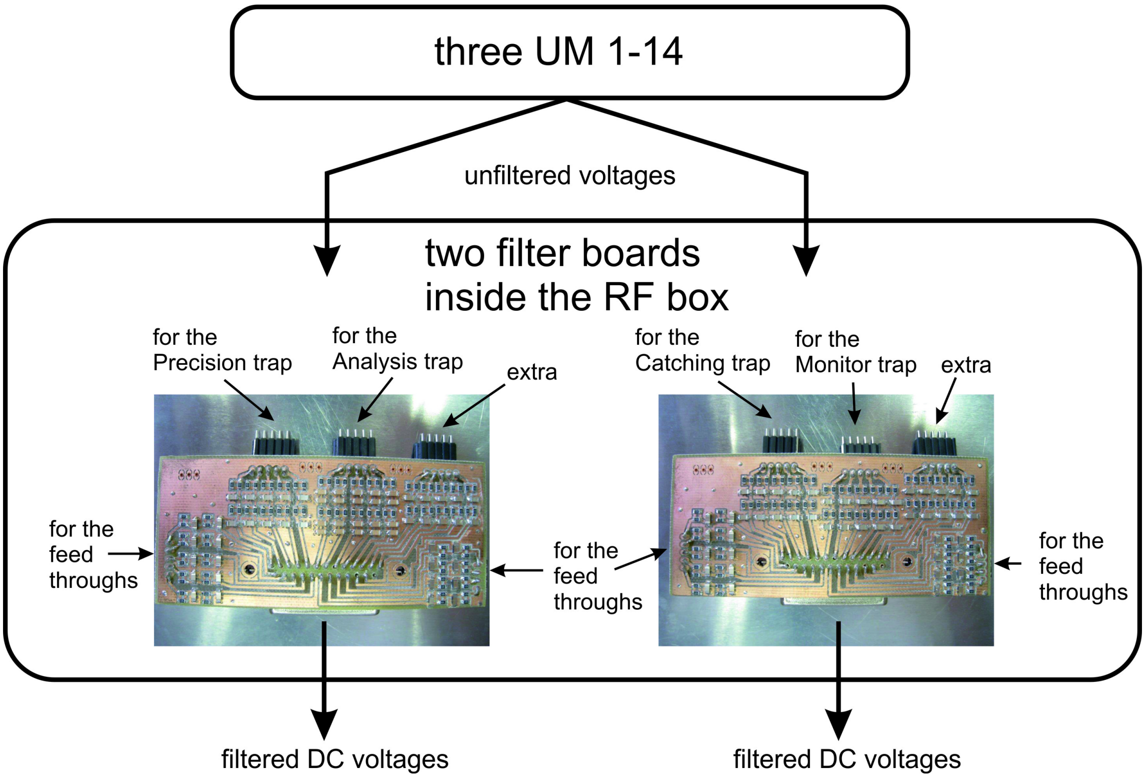

Fig. 6.7: Diagram of how voltages are cleaned by the two filter-boards. Each board consists of 24 channel RC filters. Filtered DC voltages will be transported to Penning traps.

Chapter 7

Summary and further development

§ 7.1 Summary

In my master studies, I mainly contributed to the development of highly-sensitive detection systems for the measurement of the axial oscillation frequency (600 kHz to 1 MHz) of a single trapped antiproton. Compared to previously used similar detection systems [44], the superconducting resonators have a factor of 1.5 higher unloaded parallel resistance and the cryogenic amplifiers have only 0.65 nV/$\sqrt{\text{Hz}}$ equivalent input noise. By connecting our developed detection system to a test Penning trap, we obtained SNR of 34.5 dB and Q-value of 21,000. Compared to detectors used at the BASE companion at Mainz, this indicates that the frequency scatter of the central dip obtained from the dip function is a factor of 1.3 smaller for our detection system, when the averaging time is fixed. When reversing this point of view, the measurement time for the axial frequency can be reduced by a factor of 2, which will be less sensitive to systematic drifts. The prototype detection system described in this thesis is among other developments and will be a basis to reach the goal of measuring the antiproton magnetic moment with high precision.

In addition, characterization of the ultra-high precision voltage source UM 1-14 is proceeded, and it was found that there are two voltage fluctuation ingredients; the drift caused by temperature fluctuation, and short term fluctuations due to the voltage source itself. The latter was evaluated by the normal Allan deviation, which is the most common time domain measure of stability. From the evaluation, the voltage fluctuation of 10 mHz in 30 seconds is observed, therefore, it is small enough to resolve the axial frequency shift caused by a spin flip. On the other hand, the former fluctuation was evaluated by simple algebras and obtained 3.4 μV/K. This is pointing out that the temperature stability of 0.3 mK/sec is required. To this end, the temperature stabilization apparatus was constructed.

§ 7.2 Further development

In high-precision measurements of the magnetic moment of the antiproton, the spin state of the single trapped particle is analyzed in a Penning trap with a strong superimposed magnetic bottle. The magnetic bottle couples the spin of the trapped particle to the axial oscillation frequency. A spin quantum jump shifts this axial frequency, measured via dip detection in a typical measuring time of about 60s, by 170 mHz out of 740 kHz. This requires highly stable conditions of the Penning trap potential as well as of the radial cyclotron energy of the particle. Via the magnetic bottle cyclotron energy is coupled to the axial frequency and a cyclotron quantum transition shifts the axial frequency by 63 mHz. In the current state of the art experiments the cyclotron energy fluctuates at the level of 2 to 5 cyclotron transitions per minute, leading to axial frequency fluctuations, which limit the detectability of the spin state, thus reducing experimental precision. The development and implementation of much faster, precise frequency detection techniques at time scales below the current cyclotron quantum transition rate will provide a solution to this problem. This will boost experimental precision in the magnetic moment measurement to the sub-ppb level. Specifically the application of Phase Sensitive Detection (PSD) techniques are attractive, since it is expected to measure the axial frequency on the order of 1 second.

The main feature of this method is that the axial frequency is obtained by measuring the relative phase between a defined, frequency-locked RF signal and the antiproton signal. The axial motion of the antiproton with frequency ν_z is excited resonantly with an RF drive at ν_{drive}. Afterwards, the particle is decoupled from the axial detection system for a free phase evolution time t. Subsequently, the antiproton is re-coupled to the detection system and the relative phase $\Delta\Phi$ is measured (see Fig. 7.1). From this process, the axial frequency is extracted in extremely short time ($\Delta\Phi$=360(ν_{drive}-ν_z)t), it

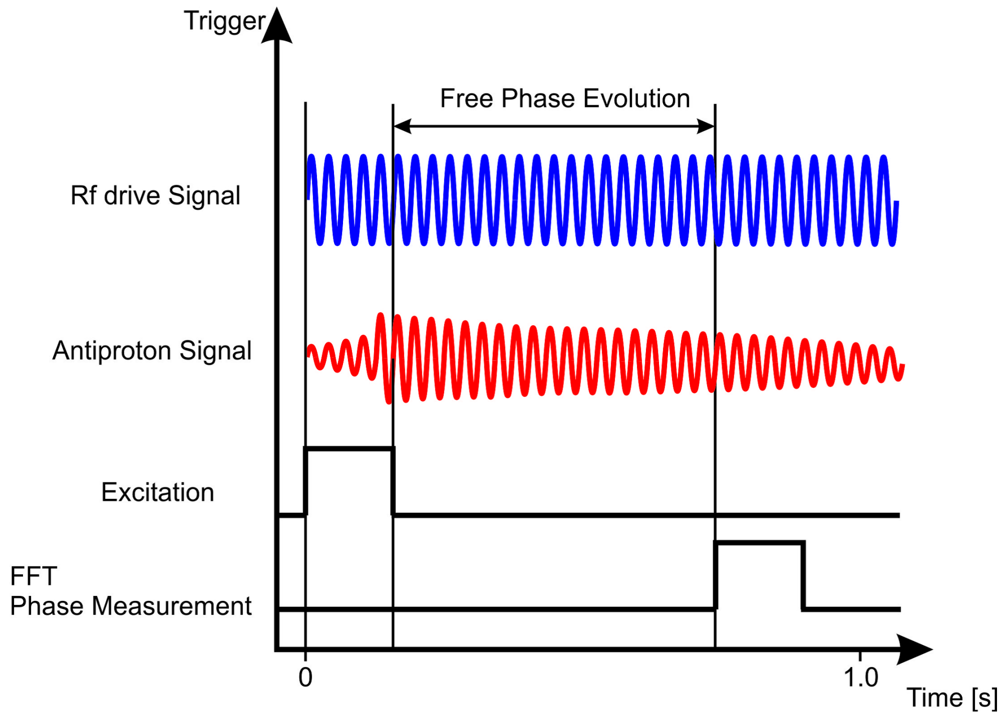

Fig. 7.1: Diagram of the Phase Sensitive Detection.

even beats the Fourier limit, since frequency and phase of the RF drive are well-known. However, the application of PSD in the strong magnetic bottle is a challenge. Spurious RF noise induced by the drive increases the cyclotron transition rate. Therefore, up to now the PSD has never applied to analyze the particle spin state. To achieve this application, the development of ultra clean frequency generators with excellent signal-to-noise ratio, implementation of a cryogenic low noise switching system into the BASE Penning trap apparatus, and the development of the complex 300K electronics system are required. In my master thesis work I developed highly sensitive detection systems for the measurement of the axial frequency of the single trapped particle. This will be the first required key component for building the basis of the successful implementation of PSD. It is expected that this technique boost the experimental precision of the (anti)proton g-factor measurement below the ppb level, which will provide one of the most stringent tests of matter/antimatter symmetry.

Chapter 8

Acknowledgement

BASEの研究に携わる貴重な機会を与えて下さいました、指導教官である松田恭幸准教授に深謝致します。研究・勉強に関することから、プライベートの悩み事まで非常に親身になって相談に乗って頂きました。先生からの支えがあったからこそ、修論研究を最後までやり遂げられたのだと思います。この場を借りて深く感謝申し上げます。山崎泰規特任教授には、CERNでの生活支援を頂き、修士一年次の夏に行われたASACUSAのビームタイムでは、反水素合成実験に必要な陽電子の制御に携わる機会を与えて下さいました。鳥居寛之助教には、CERN周辺で生活する上での豆知識から、必要な手続きについてまで、あらゆる面でサポートして頂きました。黒田直史助教には、ASACUSAの実験全般に関してご指導頂きました。研究室の先輩である大塚未来氏、田中香津生氏、高木聡氏には、日常の議論を通じて多くの知識や示唆を頂きました。また、水谷丈洋君、田島美典さんとは同輩として互いに切磋琢磨することで、充実した修士過程の二年間を送ることができました。後輩の樋口嵩君、石川彰一郎君には、私がジュネーヴで生活している間、大学院の書類手続き等で大変お世話になりました。理研秘書の和田ひとみさん、井澤真知子さんには、CERN出張手続きをはじめ、大変お世話になりました。

I would like to thank Stefan Ulmer, the team leader of the BASE collaboration at CERN, for giving me such an attractive project for my master thesis studies. I am very proud of being part of BASE members and participating in this project. I learned a lot of things about the BASE project from Stefan. Especially, I asked him numerous questions related to electronics, and he kindly taught me until I completely understood. In addition, he gave a lot of his time for correcting this thesis, even though he was quite busy with other duties. His passion and attitude toward experiments strongly influenced my motivation, which made me feel excited for participating on further experiments, especially the first beam time for BASE that will take place in 2014. I would like to thank Christian Smorra for his continuous support for my project. Not only he helped me with developing detection systems, but also helped me with data analysis as well as making LABVIEW programs. He kindly taught me from the basics, since I wasn't that much used to computer programming. Moreover, he helped me with finding an apartment near CERN when I started to live in Geneva. I would like to thank Kurt Alan Franke for teaching me many kinds of mechanical techniques. I learned machinery work mostly from Kurt. He has always been friendly and kind to anyone, making it enjoyable to work in BASE. He encouraged me frequently while I was having a hard time writing my thesis. I would like to thank Georg Ludwig Schneider, who is also a master student in BASE. I am very grateful to work with him during my master studies. He has always been serious about experiments, having many discussions with everyone. His attitude influenced me strongly as well, making me enthusiastic towards my project.

I would like to conclude this acknowledgement by thanking my family and friends, who have always supported me during my master studies.

Bibliography

[1] R. Frisch and O. Stern, Z. Phys. A: Hadrons Nucl. **85**, 17 (1933).

[2] I. Estermann and O. Stern, Z. Phys. A: Hadrons Nucl. **85**, 4 (1933).

[3] J. M. B. Kellogg, I. I. Rabi, N. F. Ramsey, and J. R. Zacharias, Phys. Rev. **56**, 728 (1939).

[4] F. Bloch, W. W. Hansen, and Martin Packard, Phys. Rev. **69**, 127 (1946).

[5] E. M. Purcell, H. C. Torrey, and R. V. Pound, Phys. Rev. **69**, 37 (1946).

[6] H. M. Goldenberg, D. Kleppner, and N. F. Ramsey, Phys. Rev. Lett. **5**, 361 (1960).

[7] T. Myint, D. Kleppner, N. F. Ramsey, and H. G. Robinson, Phys. Rev. Lett. **17**, 405 (1966).

[8] P. F. Winkler, D. Kleppner, T. Myint, and F. G. Walther, Phys. Rev. A. **5**, 83 (1972).

[9] P. J. Mohr, B. N. Taylor, and D. B. Newell, Rev. Mod. Phys. **84**, 1527 (2012).

[10] A. Kreissl et al., Z. Phys. C. **37**, 557 (1988).

[11] T. Pask et al., Phys. Lett. B. **678**, 55 (2009).

[12] J. DiSciacca et al., Phys. Rev. Lett. **110**,130801 (2013).

[13] R. S. VanDyck, P. B. Schwinberg, and H. G. Dehmelt, Phys. Rev. Lett. **59** 26 (1987).

[14] S. Sturm et al., Phys. Rev. Lett. **107**, 023002 (2011).

[15] H. Häffner, T. Beier, S. Djekic, N. Hermanspahn, H.-J. Kluge, W. Quint, S. Stahl, J. Verdù, T. Valenzuela, and G. Werth, Eur. Phys. J. D - At. Mol. Opt. Plas. Phys. **22**, 163 (2003).

[16] L. S. Brown and G. Gabrielse, Rev. Mod. Phys. **58**, 233 (1986).

[17] L. S. Brown and G. Gabrielse, Phys. Rev. A. **25**, 2423 (1981).

[18] H. Dehmelt and P. Ekström, Bull. Am. Phys. Soc. **18**, 72 (1973).

[19] I. Rabi, J. Zacharias, S. Millman, and P. Kusch, Phys. Rev. **53**, 318 (1938).

[20] A. Mooser et al., Phys. Lett. B. **723**, 78 (2013).

[21] H. Häffner, T. Beier, N. Hermanspahn, H. Kluge, W. Quint, S. Stahl, J. Verdù, and G. Werth, Phys. Rev. Lett. **85**, 5308 (2000).

[22] J. Verdù, S. Djekic, S. Stahl, T. Valenzuela, M. Vogel, G. Werth, T. Beier, H. Kluge, and W. Quint, Phys. Rev. Lett. **92**, 093002 (2004).

[23] BASE technical design report submitted to CERN, http://cds.cern.ch/record/1503514?ln=ja.

[24] H. Kalinowski, Hyperfine Interactions **76**, 73 (1993).

[25] G. Gabrielse, L. Haarsma, and S. L. Rolston, Int. J. Mass Spec. **88**, 319 (1989).

[26] G. Gabrielse et al., Phys. Rev. Lett. **63**, 1360 (1989).

[27] D. J. Wineland and H. G. Dehmelt, J. Appl. Phys. **46**, 919 (1975).

[28] S. Ulmer, H. Kracke, K. Blaum, S. Kreim, A. Mooser, W. Quint, C. C. Rodegheri, and J. Walz, Rev. Sci. Inst. **80**, 123302 (2009).

[29] J. Ketelaer et al., Eur. Phys. J. A **42**, 311 (2009).

[30] S. Ulmer, Ph.D thesis, University of Heidelberg, Germany (2011).

[31] K. A. Franke, Ph.D thesis, University of Heidelberg, Germany, to be submitted (2015).

[32] J. Johnson, Phys. Rev. **32**, 97 (1928).

[33] H. Nyquist, Phys. Rev. **32**, 110 (1928).

[34] W. Buckel and R. Kleiner, *Superconductivity* (Wiley-VCH, Weinheim, 2004).

[35] R. Kirschman, S. Lemoff, J. Lipa, and R. Experiment, Conf. Inf. Read. El. 1, 21 (1992).

[36] A. Lee, Rev. Sci. Inst. **64**, 2373 (1993).

[37] A. Robinson, V. Talyanskii, Rev. Sci. Inst. **75**, 3169 (2004).

[38] B. durso, B. Odom, and G. Gabrielse, Phys. Rev. Lett **90**, 43001 (2003).

[39] S. Ulmer, C. C. Rodegheri, K. Blaum, H. Kracke, A. Mooser, W. Quint, and J. Walz, Phys. Rev. Lett. **106**, 253001 (2011).

[40] J. DiSciacca and G. Gabrielse, Phys. Rev. Lett. **108**, 153001 (2012).

[41] G. Grandi, M. K. Kazimierczuk, A. Massarini, and U. Reggiani, IEEE transactions on industry applications. **35**, 1162 (1999).

[42] R. Nguyen, Ph.D thesis, Massachusetts Institute of Technology, USA (1998).

[43] A. Mooser, Ph.D thesis, University of Mainz, Germany, submitted (2013).

[44] A. Mooser, H. Kracke, K. Blaum, S. A. Bräuninger, K. Franke, C. Leiteritz, W. Quint, C. C. Rodegheri, S. Ulmer, and J. Walz, Phys. Rev. Lett. **110**, 140405 (2013).